

Iron Oxide Nanoparticle Coatings Dictate Cell Outcomes Despite the Influence of Protein Coronas

*Yadileiny Portilla¹, Sara Mellid^{1, #}, Alberto Paradela², Antonio Ramos-Fernández²,
Neus Daviu¹, Laura Sanz-Ortega^{1, §}, Sonia Pérez-Yagüe¹, María P. Morales³ and
Domingo F. Barber^{1, *}*

¹*Department of Immunology and Oncology and Nanobiomedicine Initiative, Centro Nacional de Biotecnología (CNB-CSIC), Darwin 3, 28049 Madrid, Spain.*

²*Proteomics Facility, Centro Nacional de Biotecnología (CNB-CSIC), Darwin 3, 28049 Madrid, Spain.*

³*Department of Energy, Environment and Health, Instituto de Ciencia de Materiales de Madrid (ICMM-CSIC), Sor Juana Inés de la Cruz 3, 28049 Madrid, Spain.*

[#] *Current address: Centro Nacional de Investigaciones Oncológicas (CNIO), Melchor Fernández Almagro 3, 28029 Madrid, Spain.*

[§] *Current address: Center for Hematology and Regenerative Medicine (HERM), Department of Medicine, Karolinska Institute, 14183 Stockholm, Sweden.*

AUTHOR INFORMATION

Corresponding Author: *E-mail: dfbarber@cnb.csic.es (D.F.B)

ABSTRACT

A critical issue in nanomedicine is to understand the complex dynamics that dictate the interactions of nanoparticles (NPs) with their biological milieu. The most exposed part of a nanoparticle is its surface coating, which comes into contact with the biological medium and adsorbs proteins, forming what is known as a protein corona (PC). It is assumed that this PC mainly dictates the nanoparticle-cell interactions. As such, we set out to analyze how different coatings on iron oxide nanoparticles (MNPs) affect the composition of the PC that forms on top of them, and how these newly formed coronas influence the uptake of MNPs by macrophages and tumor cells, their subcellular location upon internalization and their intracellular degradation. We found that different superficial charges of the coatings did not affect the PC composition, with an enrichment in proteins with affinity for divalent ions regardless of the type of coating. The iron oxide core of the MNP might become exposed to the biological medium, influencing the proteins that constitute the PCs. The presence of enzymes with hydrolase activity in the PC could explain the degradation of the coatings when they come into contact with the biological media. In terms of MNP internalization by cells, coatings mainly determine the endocytic pathways used, especially in terms of receptor-mediated endocytosis. However, the increase in hydrodynamic size provoked by the formation of the associated corona drives uptake mechanisms like macropinocytosis. Once inside the cells, the PC protected the NPs in their intracellular transit to lysosomes, where they were fully degraded. This understanding of how coatings and PCs influence different cellular processes will help design improved NPs for biomedical applications, taking into account the influence of the coating and corona on the biology of the NPs.

KEYWORDS: *protein corona, iron oxide nanoparticles, cellular nanoparticle uptake, nanoparticle coatings, protein corona degradation.*

INTRODUCTION

There has been increasing interest in nanotechnology over recent years, marked by the continued scientific and technological advances in many fields like the electronics and textile industries, and especially in medicine¹. The use of nanomaterials in biomedical applications has led to an expansion in the field of nanomedicine, leading to significant improvements in the way diseases are diagnosed and treated². Iron oxide nanoparticles are among the most intensely explored nanomaterials in nanomedicine. Based on the advantages provided by their small size and the magnetic nature of their iron oxide core, MNPs have facilitated the development of new applications in the nanomedicine field, such as the magnetic targeting of MNPs for drug release^{3, 4}, magnetic separation⁵, magnetic hyperthermia⁶ or magnetic resonance imaging (MRI)⁷. To bring such applications based on magnetic nanoparticles closer to the clinic, it is important to deepen our understanding of MNP-cell interactions, in particular those related to parameters like the nature of the nanosystem (e.g., the physicochemical properties of NPs), nanobio interfaces (e.g., the impact of the PC and coating interactions), and cell type. In this work we analyzed nanobio interfaces, specifically the interactions of MNPs with their biological environment and the impact of the MNP's coating and the PC on cellular outcomes.

Once NPs are placed in a biological medium, they rapidly adsorb proteins onto their surface. This dynamic adsorption depends on the binding affinity of the proteins in the medium to the molecules on the surface of the NPs, and the affinity of the NP-attached proteins to other proteins in the medium. These adsorbed proteins form a structure on top of the NP called the protein corona^{8, 9}. During this dynamic process, the first proteins that adhere to the NP's surface are those that are most abundant in the medium (i.e., the most abundant serum proteins), and these are replaced over time by serum proteins with higher affinity for the molecules on the NP surface, forming a layer of

tightly-bound proteins known as the “hard corona” or “inner corona”. Subsequently, other proteins then interact with this firmly bound protein-NP complex, establishing looser, low-affinity protein-protein interactions and forming the so-called “soft corona” or “outer corona”^{10, 11}. The PC that forms alters the NP’s physicochemical properties, such as its size or superficial charge, thereby affecting the stability of the NPs in culture media or biological fluids¹². In addition, these modifications also affect how NPs interact with cells, which in turn may alter their biocompatibility, their route of intracellular internalization¹³, their biodistribution¹⁴, their ability to activate immune cells¹⁵ or their final destination inside the cells¹⁶. Hence, the PC confers a biological identity to inorganic NPs and their coatings without having to perform functionalization with biomolecules or drugs, features that must be carefully studied to fully understand the biological impact of inorganic NPs¹⁷.

It has been proposed that the early stages of NP uptake by cells depends mainly on the PC formed on the NP surface¹⁸ and that this may persist at later stages of uptake, yet coatings may also be key factors in NP uptake by cells^{13, 19}. NPs are typically internalized by cells through endocytosis, which can be divided into two main mechanisms: phagocytosis and pinocytosis. Phagocytosis is used to take-up large particles, and it is the first step in the degradation of particles larger than 0.5 μm . By contrast, pinocytosis is used to internalize fluid surrounding the cell, whereby all the particles in the fluid phase in the area of invagination are taken up together^{13, 20}. Multiple endocytotic pathways exist that are distinguished by the specific molecular regulators involved. Clathrin-mediated endocytosis (CME) is by far the best studied of these mechanisms and for a long time it was believed to be the only endocytotic mechanism in addition to phagocytosis and macropinocytosis. However, more recently several mechanisms of clathrin-independent endocytosis (CIE) have been described.

These include dynamin-dependent mechanisms (RhoA and caveolin-caveolae/lipid raft dependent) and dynamin-independent mechanisms (Cdc42 dependent and Arf6 dependent). Moreover, so-called “receptor-mediated endocytosis” involves different mechanisms of endocytosis depending on the receptor involved^{20, 21}.

Studies of the cellular uptake of NPs have generally focused on three endocytotic processes: clathrin-dependent endocytosis, caveolae-dependent endocytosis, and macropinocytosis (a mechanism involved in the internalization of larger NPs). Several studies have shown that PCs influence the number of NPs that enter the cell^{13, 17, 22}, their route of entry and their subsequent cellular processing¹⁴. However, little is known about how PC composition might affect these parameters. For example, the same NPs incubated under identical conditions but with different serum concentrations, display divergent behaviors toward specific cell types depending on their PC^{22, 23, 24}.

To analyze the dynamics of PC formation in biological media, we first synthesized MNPs (12 nm core size) by co-precipitation and they were coated with three different polymers: aminopropylsilane (APS), dextran (DEX) and dimercaptosuccinic acid (DMSA). We incubated these MNPs in culture medium supplemented with 10 % fetal bovine serum (FBS) to allow a PC to form, the most common conditions used *in vitro*. We followed the variation in hydrodynamic size and superficial charge of the MNPs during the PC formation process, and subsequently, the protein pool that forms the PC associated with each type of coated-MNP was identified by proteomic analysis, comparing the protein abundance in each pool using label-free proteomics. Coating degradation after MNPs come into contact with the biological medium was evaluated by comparing the infrared (IR) spectra of MNPs before and after incubation with serum-containing medium. Finally, we evaluated whether the PC formed on each type

of coating could dictate the pathway of internalization for the MNPs and the degradation pathway of the PC inside the cells following internalization.

The results from these analyses indicate that the stabilization time for corona formation was similar for all the coatings, although the final hydrodynamic size of each type of coating once the corona was formed was significantly different. The corona composition was similar for each type of MNP, despite the differences in the superficial charge. We also observed an enrichment in divalent ion-binding proteins that might indicate that the iron oxide core could condition the selection of certain corona proteins. We noted that the coatings were degraded by their associated PC, probably due to the hydrolases present in the corona. In terms of the influence of the corona on internalization, this was determined for particles with a large hydrodynamic size, to which the PC contributes significantly. However, for other types of internalization the coating was the determining factor in triggering uptake. Finally, an analysis of corona degradation inside the cell showed it was not degraded immediately after cell uptake and that the MNPs were targeted to lysosomes. This knowledge will help to improve diagnostic and therapeutic strategies based on NPs.

RESULTS AND DISCUSSION

Different polymeric coatings provided MNPs with different surface charges. We first analyzed how MNP coatings affect the physicochemical properties of MNPs once in contact with biological media, such as the hydrodynamic diameter, the Z-potential and the PC composition. MNP cores were synthesized by co-precipitation following the protocols described in the Materials and Methods²⁵. Iron oxide cores with an almost spherical morphology were obtained by co-precipitation of iron salts in a basic aqueous

media, with $\sim 12.7 \pm 2.6$ nm (PDI- 0.17) monodispersed iron oxide cores evident in transmission electronic microscopy (TEM) images (Figure 1a). Iron oxide cores were then coated with APS or DEX polymers, or with DMSA, to produce a positive, neutral or negative surface charge, respectively. When studied by dynamic light scattering (DLS), the APS-coated iron oxide cores (APS-MNPs) had a surface charge of +23 mV, while DEX-coated iron oxide cores (DEX-MNPs) proved to be close to neutral (-1.8 mV). Conversely, DMSA-coated iron oxide cores (DMSA-MNPs) had a negatively charged surface (-34 mV) at pH 7 (Table 1). The corresponding hydrodynamic size of the APS-, DEX- and DMSA-MNPs was 122 nm, 109 nm and 83 nm, respectively. Hence, in addition to producing different surface charges, these coatings moderately affected the final MNP size (± 39 nm: Table 1). The degree of polydispersity was seen to be approximately 20% in TEM images, indicating that all the coated-MNPs were fairly well monodispersed.

To quantify how much polymer was bound to the iron oxide core of the MNPs, a thermogravimetric (TG) analyses was performed. The mass percentage of the coatings varied from 38% for DMSA-MNPs and 18% for APS-MNPs to about 10% for DEX-MNPs. Moreover, the presence of characteristic IR bands detected by Fourier-transform infrared spectroscopy (FTIR) confirmed that MNPs were coated with the corresponding organic compounds (Figure 1b): 2930 and 998 cm^{-1} for APS; 2900 and 1450-918 cm^{-1} for DEX; and 1625 and 1383 cm^{-1} for DMSA. Fe-O bond-specific IR bands at 500-600 cm^{-1} were detected in all cases, and the 1381 cm^{-1} band in the APS-MNPs spectra is due to the nitric acid used during MNP oxidation and pH adjustment. Powder X-ray Diffraction (XRD) produced the characteristic pattern of the inverse spine structure compared to the $\gamma\text{-Fe}_2\text{O}_3$ phase (ISCD-084611: Figure 1c). Finally, the

magnetization measurements confirmed the superparamagnetic behavior of the MNPs at room temperature (RT: Figure 1d).

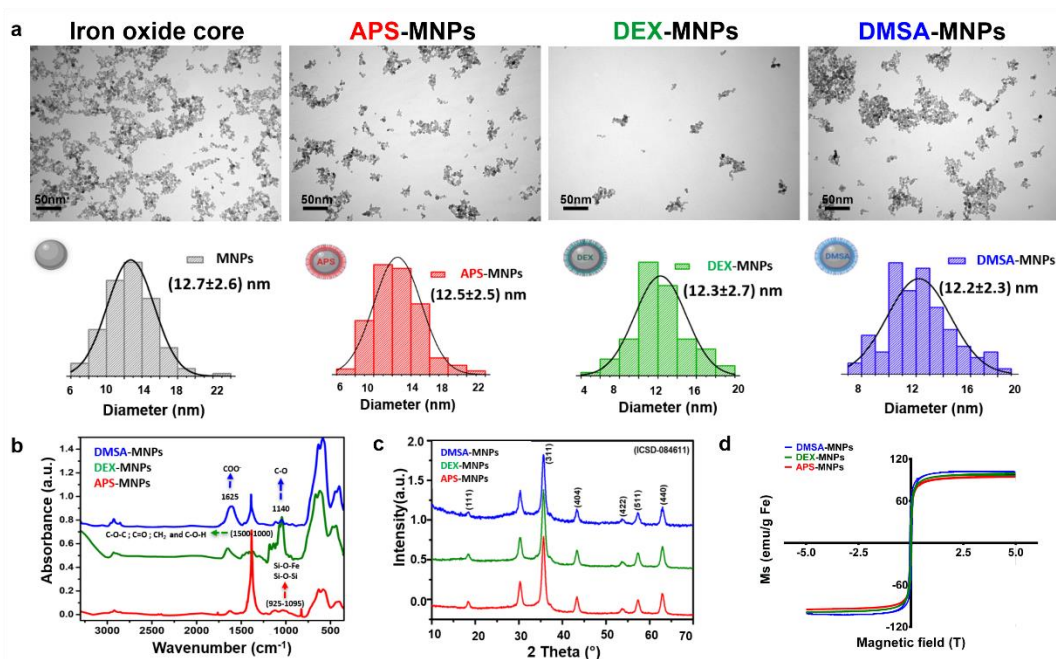


Figure 1. Physicochemical characterization of MNPs. (a) TEM images of iron oxide cores prepared by co-precipitation (*top*), and MNP size distribution and Gaussian fitting (*bottom*). TEM images of coated APS-, DEX- and DMSA-MNPs. (b) Fourier transformed infrared spectra of the MNPs. (c) X-ray diffraction pattern of the MNPs. (d) Magnetization curve at RT for the MNPs showing the superparamagnetic behavior. Scale bar: 50 nm.

Table 1. Summary of the main physicochemical characteristics of APS-MNPs, DEX-MNPs and DMSA-MNPs

MNPs	Coatings	% Coatings	Hydrodynamic diameter (nm)	Z-potential (mV)
APS-MNPs	(3-aminopropyl) triethoxysilane	18.3	122.4	+23
DEX-MNPs	dextran 6KDa	9.9	109	-1.8
DMSA-MNPs	dimercaptosuccinic acid	38.3	82.8	-34.3

Characterization of the PC formed on MNPs with different coatings. When the MNPs are placed in medium containing serum, they rapidly adsorb proteins from the medium that form a PC on top of the MNPs, increasing the hydrodynamic size of the MNPs. As mentioned in the introduction, PC formation takes time and it involves the

initial binding of the more abundant proteins in the milieu, which are then gradually replaced by proteins with higher affinity for the molecules at the MNP surface, these tightly-bound proteins forming the hard or inner corona. Subsequently, other proteins interact with these inner corona proteins, establishing looser bonds and lower affinity protein-protein interactions, and forming a second layer known as the soft or outer corona.

To evaluate the effect of the different coatings on PC formation, APS-, DEX- and DMSA-MNPs were incubated *in vitro* for different times (0, 1, 3, 5, 10, 24, 48 and 72 h) in Dulbecco's modified Eagle medium (DMEM) supplemented with a standard concentration of FBS for cell culture (10%). The kinetics of PC formation was characterized by measuring the change in hydrodynamic size and the Z-potential values of each type of MNP over time. As expected, the distinct coated MNPs increased their hydrodynamic size in medium containing FBS (Figure 2a and Figure S1a). The PC formation dynamics revealed that coated MNPs reach their maximum hydrodynamic size after a 5-10 h incubation (2455 nm for APS-MNPs; 438 nm for DEX-MNPs; and 209 nm for DMSA-MNPs), decreasing thereafter until it stabilized after 24 h (Figure 2a). After 24 h, the steady hydrodynamic diameter may reflect the equilibrium in dynamic protein exchange at the surface of the MNPs. The increase in size observed in the presence of FBS can be explained by the formation of a PC around the MNPs rather than their aggregation, with the DLS analysis reflecting a monodisperse profile (a single peak) over time (see Figure S1: Characterization of the stability of MNPs over time). Nonetheless, we cannot rule out some degree of hetero-aggregation, principally in the APS-MNPs, because the hydrodynamic peaks of the MNPs incubated in medium with FBS had a wider distribution than those of the MNPs incubated in medium alone (Figure S1a). To evaluate the proportion of tightly-bound proteins *versus* loosely-bound

proteins in the PC formed, we detached the loosely adsorbed proteins by washing and centrifugation of NPs^{10, 26}, quantifying the proteins in the supernatants from these washes (outer corona) and those in the MNP fraction (re-dispersed MNPs after being washed) that were the more stably attached proteins. The hydrodynamic size analysis of MNPs before and after elimination of the loosely-bound proteins (Figure 2a) showed that the maximum hydrodynamic size for each type of coating was smaller after 5-10 h when the loosely-bound proteins had been washed off the MNPs (1737 nm for APS-MNPs; 301 nm for DEX-MNPs; and 176 nm for DMSA-MNPs). The proportion of these loosely-bound proteins was reduced and it remained stable at later time points when a more stable hydrodynamic diameter was evident, indication of the formation of a stable corona. When the proportion of proteins loosely attached relative to those stably attached to MNPs was quantified (Figure 2b), the higher hydrodynamic size was correlated with a higher proportion of loosely-bound proteins in the PC. By contrast, the proportion of tightly-bound proteins relative to the loosely-bound proteins remain stable when the PC size stabilized at later time points.

Consistent with the marked increase in hydrodynamic size observed in our experiments after incubation in DMEM containing FBS, it has been reported that 15 nm Au NPs incubated in DMEM supplemented with 10% FBS for 48 h formed larger PCs (from a 20 nm mean diameter without FBS to 200 nm with FBS, ~10-fold increase) than those formed on NPs incubated in RPMI supplemented with FBS for 48 h (from a 20 nm mean diameter to 40 nm, ~2-fold increase). Moreover, PC formation in DMEM is time-dependent²⁷ and not an immediate event but rather, a dynamic process. Indeed, the stabilization of this dynamic process can take from minutes to days²⁸. Furthermore, the factors identified that influence this stabilization were the incubation medium and the serum concentration²⁹.

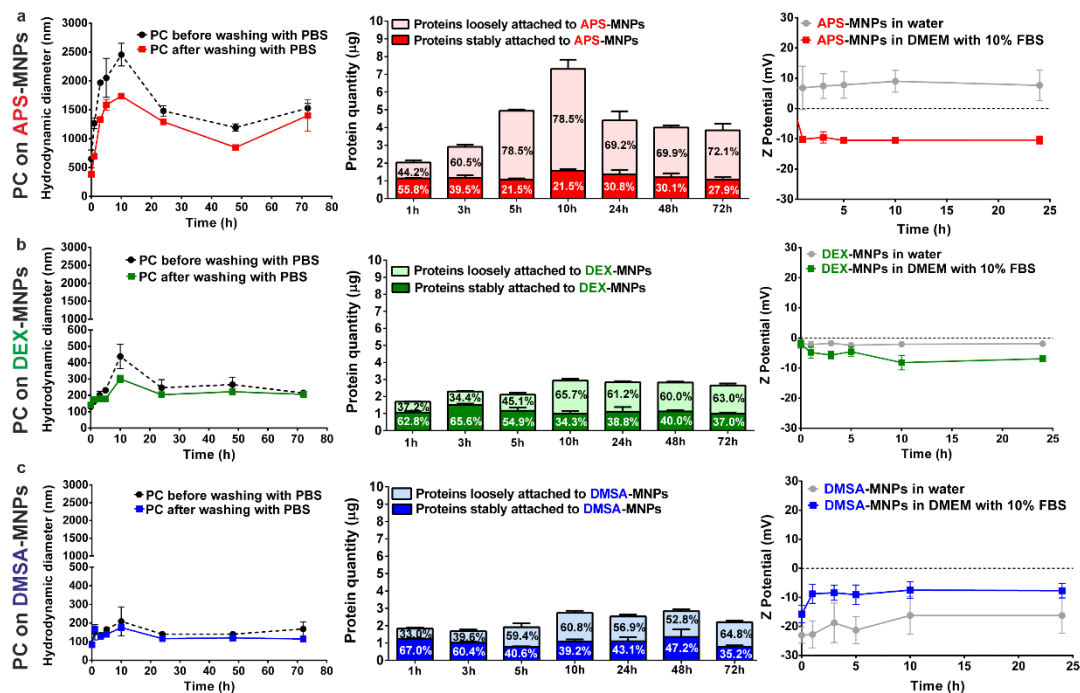


Figure 2. Analysis of the dynamics of PC formation on APS-MNPs, DEX-MNPs and DMSA-MNPs in DMEM plus 10% FBS. (a) The hydrodynamic size of APS-, DEX- and DMSA-MNPs over time as determined by DLS before and after removing the loosely attached proteins. (b) Quantification of the total amount of protein attached to MNPs, and of the proportion of loosely attached proteins relative to the proteins stably attached to the MNPs. (c) The Z-potential measured over time for the MNPs. *PC before washing with PBS*: MNPs incubated in DMEM with 10% FBS. *PC after washing with PBS*: MNPs incubated in DMEM with 10% FBS and then washed with PBS, centrifuged and resuspended in PBS. DLS measurements were performed in triplicate to determine the Z-Potential and hydrodynamic size of the MNPs.

In all three of the coated MNPs analyzed, the Z-potential was negative in medium with 10% FBS, a result of the formation of a PC in the presence of FBS (Figure 2c). Positive Z-potential values of APS-MNPs were observed in the absence of FBS (+23 mV), while when FBS was present in the medium the Z-potential values shifted to negative values. For DEX-MNPs, the Z-potential values in the sample without FBS were close to zero (-1.8 mV), whereas negative Z-potential values were observed in the presence of FBS. These variations in the Z-potential values may reflect the contribution of proteins in FBS to the PC formed, adding to their negative charge and increasing their negative Z-potential values. In the case of DMSA-MNPs, Z-potential values were negative in both conditions (with and without FBS), and while this value was -34 mV in the absence of FBS, the Z-potential values were less negative in the presence of FBS.

Hence, DMSA-MNPs would appear to bind proteins with hydrophobic residues due to their negative Z-potential value.

The differences in the increases in hydrodynamic size between the MNPs coated with different polymers after incubation in medium containing 10% FBS could be explained by the surface charges contributed by each coating. Indeed, the largest increase after 24 h (~6 fold) was observed in APS-MNPs, from 232 to 1293 nm. In DEX-MNPs this increase was ~1.5 fold, from 134 to 204 nm, and the change in size of DMSA-MNPs was ~1 fold, from 88 to 117 nm. This data is consistent with previous indications that NPs with an initially positive surface charge have larger PCs after incubation than MNPs with an initially negative surface charge³⁰.

We observed a correlation between the increase in the hydrodynamic size of coated-MNPs due to PC formation and the surface charge provided by each coating. Positively charged coatings favor a larger increase in hydrodynamic size due to PC formation, similar to the temporal evolution in the protein-NP complex observed previously³¹. Indeed, the hydrodynamic diameter of Au-NPs increased from 30 nm in the absence of an associated PC to 283.5 nm when incubated with a protein lysate for 5 minutes. The size decreased to 72.31 nm after 1 h and it stabilized after 24 h to a size of 59.2 nm. In terms of the surface charge, the Z-potential value for the Au-NPs without a corona associated was -43 mV and after 24 h, when the corona had stabilized, its Z-potential value was -8.4 mV. Accordingly, we observed a reduction in the Z-potential value for our DMSA-MNPs from -34 mV without the PC to -8 mV after a 24 h incubation with serum (Figure 2c). When incubated in medium with FBS polyvinyl alcohol (PVA) coated-NPs with different modifications, PVA-NH₂ coated-NPs, with a positive superficial charge, tended to bind a significantly larger number of serum proteins to their surface (e.g. Seroalbumin) than PVA-COOH coated-NPs, with a negative charge,

the latter binding mainly apolipoproteins and complement proteins³⁰. This influence of superficial charge on binding tendencies meant that PVA-NH₂ coated-NPs had an appreciable larger hydrodynamic size than the PVA-COOH coated-NPs, reflecting the correlation between superficial charge and hydrodynamic size. These findings support our observations and in a similar scenario, the positive superficial charge of our APS-MNPs was associated with a hydrodynamic size approximately 10 times larger than the corona of DMSA-MNPs that have a negative superficial charge.

Analysis of the composition of the PC formed on the MNPs coated with different polymers after incubation with medium containing FBS. A proteomic approach was adopted to identify and quantify the proteins that made up the PC, and to evaluate how the coatings responsible for the different surface charge of the MNPs influence the PC's composition. As such, the coated MNPs were incubate in DMEM with 10% FBS for 24 h, conditions under which the PC formed was considered to be stable (Figure 2b). After incubation, the MNPs were recovered magnetically and the unbound proteins removed by gently washing with phosphate buffered saline (PBS). Subsequently, the MNPs were resuspended in a protein extraction buffer to detach the PC proteins. These protein extracts were resolved by denaturing SDS-PAGE, trypsin digested, and the tryptic peptides were identified and quantified using a label-free proteomic approach. (Figure 3a). The proteins in the commercial FBS used here were also identified and quantified in a similar manner as a control for our analysis.

To analyze the MS/MS spectra obtained, raw data were converted to mgf files using Peak View v1.2.0.3, which was then used to search a composite target/decoy database built from the *Bos Taurus* database and downloaded from UniprotKb using Mascot Server 2.5.1, OMSSA 2.1.9, X!TANDEM 2013.02.01.1 and Myrimatch 2.2.140. This

analysis provided a list of the proteins present in the FBS serum and in the different PCs corresponding to APS-, DEX- and DMSA-MNPs. We identified 121 different proteins in FBS (see Figure S2 in the Supporting Results and Discussion, SI), including 20 that were highly abundant (see Table S1 and Figure S3 in the Supporting Results and Discussion, SI).

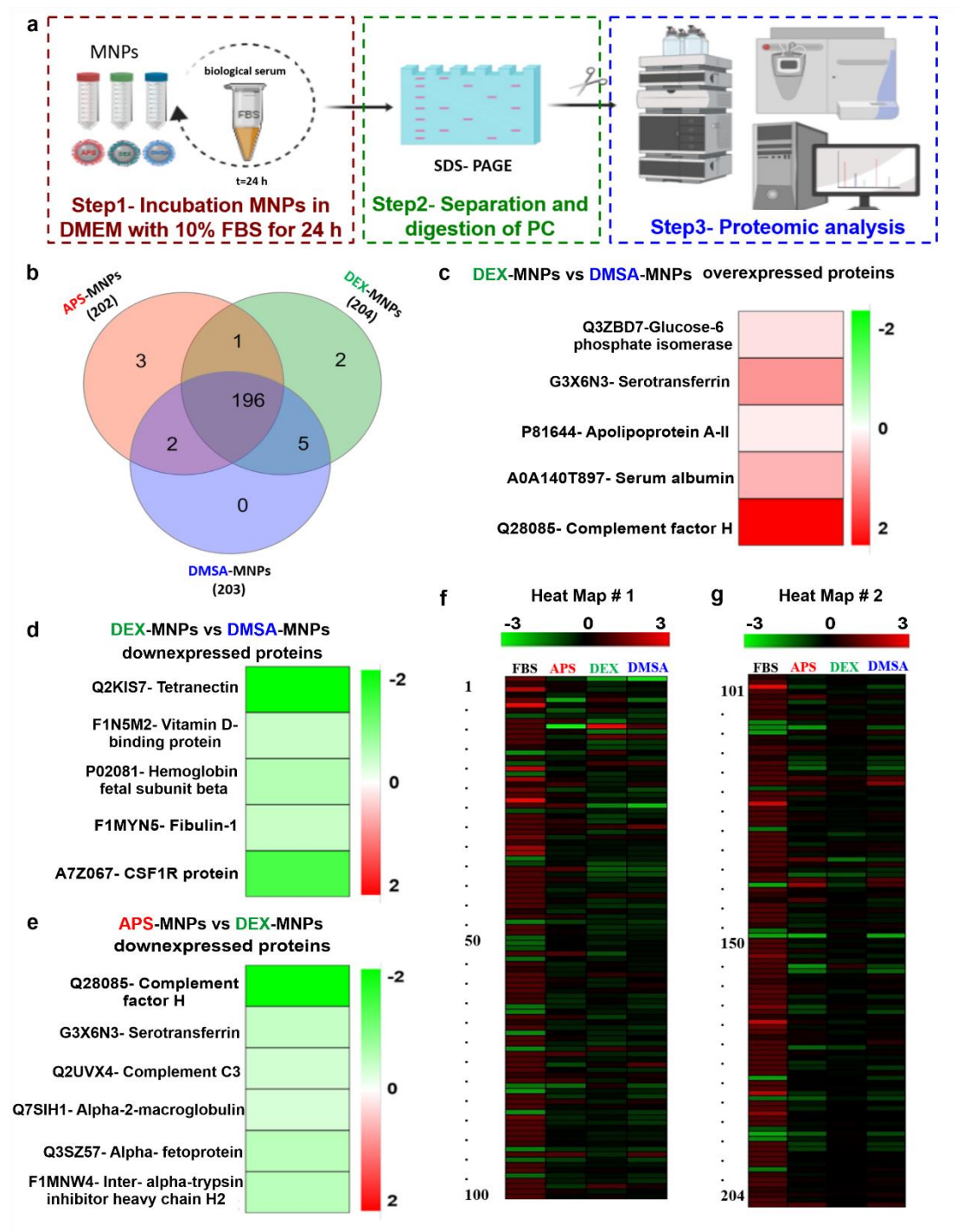


Figure 3. Proteomic characterization of the MNP's PC. (a) Scheme showing the mass spectrometry identification and quantification of the proteins in the PCs. (b) Venn diagrams representing the common and exclusive proteins identified in the PCs associated with each type of MNP. (c) Heat map of the proteins overexpressed in the DEX-MNP PCs as opposed to those on DMSA-MNP PCs. (d, e) Heat map of the downregulated proteins in the DEX-MNP PCs as opposed to those on DMSA-MNPs, and of those on the APS-MNPs as opposed to DEX-MNPs, respectively. (f, g) Relative abundance of the proteins identified in FBS and of the proteins identified in the corona, quantified by label-free proteomic analysis: Heat Map # 1 includes a total of 100 proteins; Heat Map # 2 includes a total of 104 proteins. The color of the labels indicates the fold change. In Table S3 there is a list with the name of the proteins identified.

To compare the composition of the PCs associated with the different coatings, the InteractiVenn³² software was used to examine the proteins identified as part of the PC formed on APS- (202 proteins), DEX- (204 proteins) or DMSA-MNPs (203 proteins). This analysis of the proteins in each PC showed that approximately 96% of them (196 proteins) were common to the PCs formed on all three types of coatings. In terms of their relative abundance, this parameter was similar between APS- and DEX-MNPs (85.2%), between APS- and DMSA-MNPs (80.4%), and between DEX- and DMSA-MNPs (81.2%), yet there was no correlation between the proteins most abundant in FBS and in the PCs associated with MNPs (Figure 3f, g). Based on these results, the proteins in the coronas that associate with each of the coatings are clearly similar, both in terms of composition and abundance (see Table S3: List of all the proteins identified in the coronas). Although it was not the case here, it should be noted that other studies have established close relationships between coatings and the associated PC, with significant differences in both the composition and relative abundance of proteins in the corona depending on the physicochemical characteristics of the NP^{30, 33, 34}. Indeed, an analysis of Au-NPs with different coatings (Au-citric-NP, Au-phosphine-NP, Au-PMA-NP, Au-PEG-SH-NP, and Au-PMA-sat PEG-NP) indicated that their colloidal stability in complex biological media is an important factor influencing the formation and composition of the PC³⁴. In fact, several reports suggest that the PC can be predicted from the surface chemistry of NPs^{34, 35}.

Having established the similarities between the coronas associated to each of the NP coatings, we focused on identifying the main differences. In terms of composition, there were only 2 proteins unique to APS- and DMSA-MNP coronas, 1 protein unique to APS- and DEX-MNP coronas, and 5 proteins unique to the DEX- and DMSA-MNP corona (Figure 3b). A previous proteomic characterization of the PC composition on NPs coated with glucose or polyethylene glycol (PEG) by also found that 78% of the PC proteins identified (238 proteins) were common to both¹⁴, with only 29 proteins associated exclusively to PEG-coated NPs and another 45 to glucose-coated NPs. The degree of similarity among the three coronas studied here was even higher, with 3 and 2 proteins exclusively associated with APS-MNPs and DEX-MNPs, respectively (out of 202 and 204 proteins, respectively: Figure 3b).

Focusing on these exclusive proteins, we tried to find a correlation between their structure, function or activity that could explain their unique presence on a given coating (Table 2). We used the Uniprot database (identifier in parenthesis) to obtain the information for each individual protein and the Prot pi-protein software tool to calculate the corresponding net charge (see Figure S4, and Table 2 for the proteins found exclusively in the APS- and DEX-MNPs following a Venn diagrams analysis). We observed a pattern that might explain the selective binding of the proteins, most of which showed affinity for divalent metals (Table 2). Furthermore, we also observed a correlation between the superficial charge of the coating and the charge of the binding proteins in the case of APS-MNPs.

Regarding the relative abundance, a label-free proteomic analysis served to quantify the expression of these aforementioned proteins. When both the proteins pools identified in APS- and DEX-MNP coronas were compared, 6 proteins were downregulated and none were overexpressed (Figure 3e). A similar comparison

between the protein pools corresponding to the APS- and DMSA-MNP coronas failed to identify significant differences in protein expression. Finally, when the pool of proteins corresponding to DEX- and DMSA-MNP coronas were compared, 5 down-regulated and 5 overexpressed proteins were detected (Figure 3c, d, for a statistical analysis see Supporting Information, Table S2).






Table 2. Proteins found exclusively in APS-MNPs and DEX-MNPs by Venn diagrams analysis

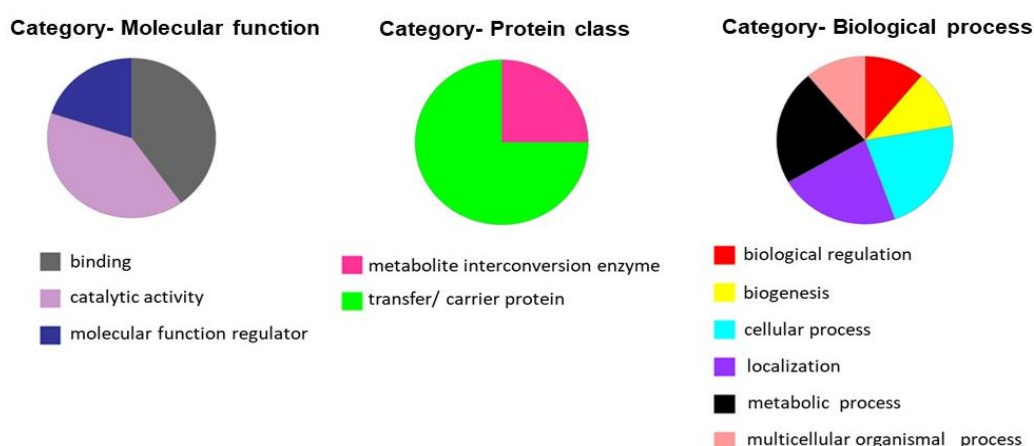
Exclusive proteins identified in APS-MNPs and DEX-MNPs				
MNPs	UniProt ID	Protein's name	Net charge	Molecular function
APS-MNPs	P81947	Tubulin alpha 1B chain	-25.616	Structural constituent of the cytoskeleton
	F1N5U1	G2/M-phase specific E3 ubiquitin protein ligase	-4.544	Zinc ion-binding
	M0QVY0	IF rod domain-containing protein	+1.738	Constituent protein of the cytoskeleton
DEX-MNPs	Q9XSJ4	Alpha-enolase	-3.289	Magnesium ion-binding
	O02659	Mannose-binding protein C	-6.656	Calcium dependent protein binding

We then analyzed the proteins overexpressed in the three PCs using the Panther gene list software, which recognizes Gene Ontology annotations and associates them with the proteins identified (Table 3). The analysis centered on 3 main categories: Molecular function, Protein class, and Biological process. Of the overexpressed proteins Serum albumin and Apolipoproteins (Apolipoprotein A-I) were found in abundance in the serum, which may explain their overexpression. However, Serotransferrin,

Complement factor H and Glucose-6-phosphate isomerase were not abundant proteins in the serum and thus, we focused on these proteins to formulate a plausible hypothesis that justifies their affinity for the surface of DEX-MNPs (Figure 3c).

Table 3. Overexpressed proteins found by comparing the DEX-MNPs and DMSA-MNPs as determined by Label-Free Proteomics

Proteins overexpressed in DEX-MNPs versus DMSA-MNPs		
ID-UniProt	Proteins name	Gene ontology term
G3X6N3	Serotransferrin 	(GO:0008199) ferric iron binding (GO:1990459) transferrin receptor binding (GO:0034986) iron chaperone activity
Q28085	Complement factor H 	(GO:0006957) complement activation, alternative pathway
A0A140T897	Serum albumin 	(GO:0008270) zinc ion binding (GO:0019825) oxygen binding (GO:0009267) cellular response to starvation
P81644	Apolipoprotein A-II 	(GO:0015485) cholesterol binding (GO:0008203) cholesterol metabolic process (GO:0002740) negative regulation of cytokine secretion involved in immune response
Q3ZBD7	Glucose-6-phosphate isomerase 	(GO:0048029) monosaccharide binding (GO:0005125) cytokine activity (GO:0051156) glucose 6-phosphate metabolic process



As for the downregulated proteins, we observed significant differences between APS- and DEX-MNPs (6 downregulated proteins), as well as between DEX- and DMSA-MNPs (5 proteins). Proteins abundant in serum, such as Tetranectin, were less abundant

in DEX- and APS-MNPs, indicating that its binding is not associated with the relative abundance of the protein in the serum.

Some differences in protein composition were noted regardless of the aforementioned similarities. Although there was no significant over-representation of any proteins in the PC formed on APS-MNPs, some very negatively charged proteins were detected: Serum albumin (-17.254), Coagulation factor IX (-13.318) and Tubulin alpha 1B chain (-25.616). Hemoglobin fetal subunit beta (-1.575) and Tetranectin (-5.579) were identified in the PC formed on DMSA-MNPs, both with hydrophobic residues in their structure. A more diverse pattern of FBS proteins was identified with DEX-MNPs and since the DEX coating provides an almost neutral charge to the MNP surface, the corona proteins were unlikely to be selected by ionic interactions but by other mechanisms (see Figure S4).

Together, this analysis showed that a significant number of the PC proteins have affinity for divalent ions. To determine if this over-representation correlates with their representation in FBS or if it reflects preferential recruitment, we compared the annotated molecular functions of the corona proteins detected in both the serum DEX-MNPs using the Panther Gene List. The corona of the DEX-MNPs was selected because it is that which has the most diverse composition and expression. We noted that 40% of the proteins present in the serum share a “binding function” and 7% of them had an “ion binding function”. Likewise, the 42.9% of the proteins of the DEX-MNP PC share a “binding function” but in contrast to the serum, 20% of these proteins exhibit an “ion binding function”, suggesting a PC enrichment of “ion binding” proteins (Figure 4, Binding function). This enrichment may reflect the contribution of the iron ions on the MNP surface to the selection of the PC proteins. Indeed, the Panther Gene List software

analysis of the annotated molecular functions for the proteins identified in the corona of DEX- and APS-MNPs showed that differentially expressed proteins had a binding specificity for divalent ions, such as iron, zinc, magnesium and calcium. Therefore, we hypothesized that many of the serum proteins that form the MNP coronas can chelate iron at the surface of the NP due to non-homogeneous coating or enzymatic degradation of the coating.

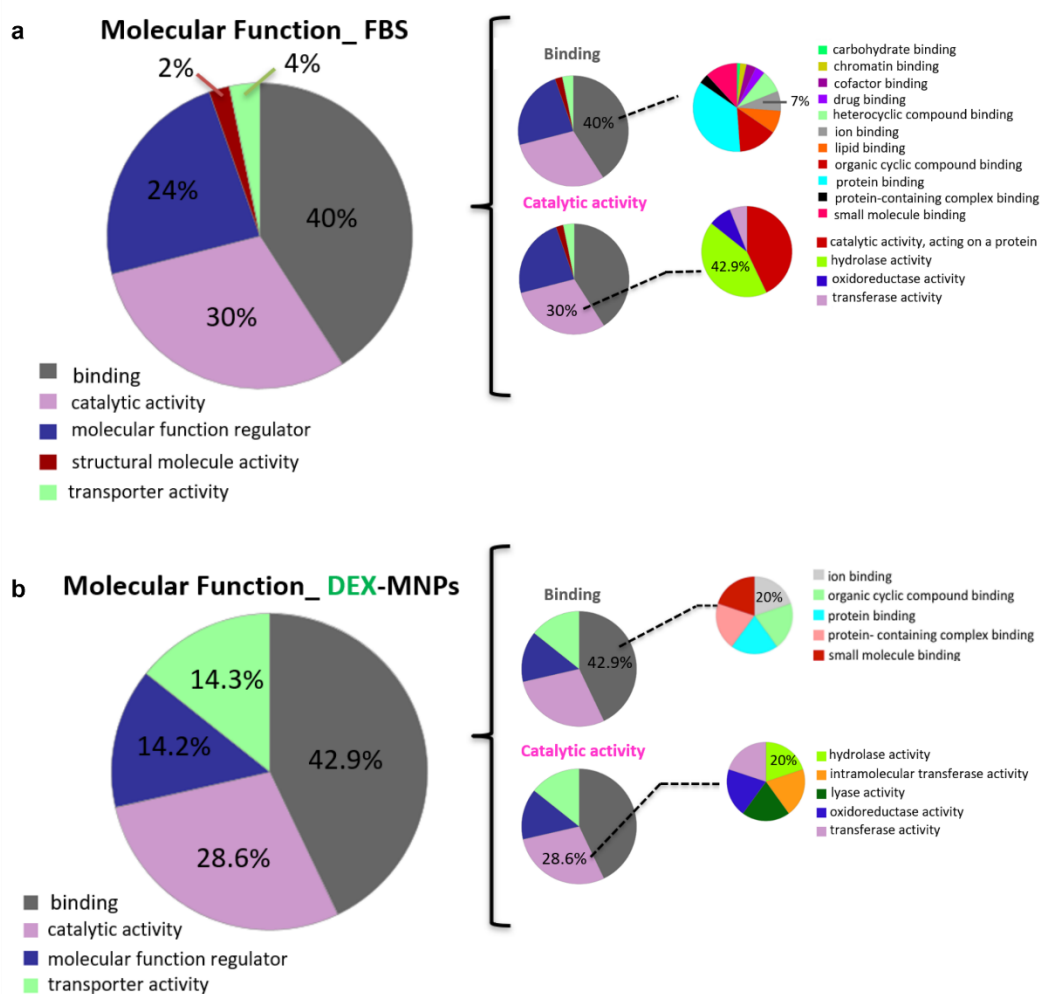


Figure 4. Comparison of the distribution of the “molecular function” of proteins identified in FBS and in the PC formed on DEX-MNPs. (a) Graph showing the percentage of proteins identified in FBS that belong to a certain “molecular function” group. (b) Graph showing the percentage of overexpressed proteins identified in the corona on DEX-MNPs that belong to a certain “molecular function” group. Different “molecular functions” are shown in different colors. The graphs in this figure were generated by the Panther Gene List software with an emphasis on binding and catalytic activity.

In the case of the DEX-MNPs used here, a theoretical calculation based on their TG analysis showed that the proportion of the coating was approximately 10% (Table 1), resulting in approximately 49 molecules of dextran per particle. Thus, given the size of the particles (12 nm diameter) and the Dextran molecule (1.8 nm chain length), and considering a random organization of the chains of this branched polysaccharide on the NP surface (occupying a maximum surface of $1.8 \times 1.8 \text{ nm}^2$), the minimum number of dextran molecules needed to cover the NP surface is around 140 (see Section: Theoretical calculations from the TG data to see if the relative coating of the APS-MNPs, DEX-MNPs and DMSA-MNPs is sufficient to form a monolayer around the iron oxide core in the Supporting Results and Discussion, SI). Therefore, if the proportion of the particle coated was less than 10%, DEX-MNPs could present uncoated areas and thus, ions from the iron oxide MNP core could be directly exposed and interact with serum proteins. In the DEX-MNP PC there were more proteins with affinity to divalent metals than in the APS- and DMSA-MNPs, further evidence that the iron oxide core of the MNPs actively selects proteins to form the corona. It has been proposed that the distribution of dextran molecules on the surface of ferumoxide particles (a commercial formulation for MRI) was not particularly uniform³⁶, provoking core exposure and associated side effects. Indeed, zones of the iron oxide core of the NPs were left uncovered³⁷, as witnessed by the identification of proteins like HPRG and kininogen-1 in the corona which have a strong binding affinity for the iron oxide core of the NPs through their histidine-rich motifs. Other proteins like b-2 glycoprotein³⁸ and apolipoprotein B³⁹ are also known to have strong affinity to the iron oxide core, consistent with our observations.

In addition to gaps in the MNP coating due to non-homogeneous polymer distribution during MNP synthesis, it is plausible that some of the serum proteins absorbed on the

MNP surface as a part of the PC have enzymatic activities that might participate in the degradation of the MNP coating. Indeed, the functional proteomic analysis (Figure 4, Catalytic activity function) indicated that 28.6% of the proteins that form the corona have “catalytic activity”. Among these, 20% corresponded to hydrolases that could participate in the degradation of the coating when MNPs were incubated in medium with serum.

The contribution of the PC to coating degradation. To study how the formation of a PC on the different coatings might degrade each coating over time, we analyzed the status of each type of MNP coating (APS, DEX and DMSA) after a 24 h incubation in medium with 10% FBS using FTIR. After incubation of the MNPs in medium containing serum to allow PC formation, the MNPs were magnetically separated from the medium containing serum and washed three times with a high salt buffer to remove as much protein as possible from the PC formed on top of the coating (see Supporting Materials and Methods, and Figure S5). After washing, the integrity of the MNP coatings was analyzed by IR. Moreover, the MNPs were also analyzed by IR before incubation in the medium containing FBS to obtain the spectra of the undegraded coatings (Figure 5). As such, the IR spectra before and after incubation in FBS containing serum could be compared.

For APS-MNPs incubated in 10% FBS, we observe three bands at 1642 cm^{-1} , 1532 cm^{-1} and 1052 cm^{-1} with a higher intensity compared to the APS-MNPs spectrum before the incubation. The first two peaks correspond to asymmetric and symmetric deformations of amino groups ($-\text{NH}_2$) and the third peak corresponds to C-N bond, probably caused by the large amount of proteins absorbed by the MNP surface during the formation of the PC. On the other hand, we can see that the Si-O bond (926 cm^{-1}) due to the APS coating was reduced in the sample incubated with the FBS for 24 h,

which could suggest partial degradation of the coating (Figure 5a).

For DEX-MNPs incubated in 10% FBS, we observed a decrease in the peaks around 1150 cm^{-1} and 1350 cm^{-1} assigned to C-O and C-H which indicates degradation of the dextran alcohols in the sample incubated in the serum for 24 h, compared to the sample obtained before incubation (Figure 5b).

Finally, for DMSA-MNPs incubated in medium with 10% FBS we analyzed the peaks at 1611 cm^{-1} assigned to C=O and no relevant changes were observed with respect to the samples taken before the incubation apart of a slight shift of the peak to 1657 cm^{-1} that could indicate the evolution of some carboxyl groups to amides (Figure 5c). This indicates that there is less degradation of this coating than of the other coatings, probably due to the smaller hydrodynamic size of DMSA-MNPs. In summary, these results show that the three coatings analyzed were degraded over time when MNPs enter into contact with medium supplemented with serum and during PC formation. It is possible that part of the signal in the peaks corresponds to amino, C-H or C-O bonds in the IR spectra, to which there may be a contribution from the bonds belonging to amino acids of unwashed proteins that remain attached to the coating before IR analysis. We calculated the percentage of proteins that remain attached to the MNP coatings after these washes (Supporting Materials and Methods), showing that only around 20% of the proteins in the PC remained attached to MNP coating before the IR analysis (Supporting Results and Discussion, Figure S5). Therefore, we cannot rule out a contribution of these proteins to the IR peaks of the amino, C-H and C-O groups. However, it should be noted that the changes observed in APS-MNP with respect to the Si-O bond group (926 cm^{-1}) reflected the partial degradation of this coating.

medium greatly accelerates the degradation of the NPs. Indeed, we found hydrolase enzymes to be present in FBS and in the PC, which could contribute to the degradation of the polymeric MNP coating. The enhanced degradation of the MNP-coating in the presence of FBS was confirmed by analyzing the IR spectra, where a shift was produced in the typical peaks associated with different coatings, mainly for DEX and APS. Finally, our MNPs are all spherical and despite the relatively short incubation with only FBS (24 h), notable degradation of the coatings was detected (Figure 5a, b).

Different groups of proteins have been shown to bind to DEX-coated NPs³⁷, the first including proteins with strong affinity for the iron oxide core. A second set of proteins bound directly to the DEX polymer and included mannose-binding lectins (MBLs) A and C proteins. MBLs are known to bind strongly to mannose polysaccharides on bacterial surfaces but they may also interact with the D-glucose units of the dextran polymer. The last group identified corresponded to proteins with weaker binding, which suggests that they may bind indirectly to the corona of the DEX-coated MNPs. This latter group included coagulation factors XI and XII, and MBL-associated serine proteases MASP-1 and 2. In conjunction with the results presented here, it seems likely that three groups of proteins in the PC associate with iron oxide coated-MNPs: proteins that show affinity for the iron oxide core (iron oxide core binders); proteins with affinity for the polymeric coating (coating binders), which can be further divided into a subsets (a) of proteins with enzymatic activity that can degrade the polymeric coating (hydrolase enzymes) and a subset (b) with electrostatic or chemical affinity for the coating (other proteins); and finally, a third group of proteins that bind to the corona more weakly through protein-protein interactions, binding to the proteins of the first or second group (secondary binders). This latter group of proteins could be related to the “soft corona” (Figure 6).

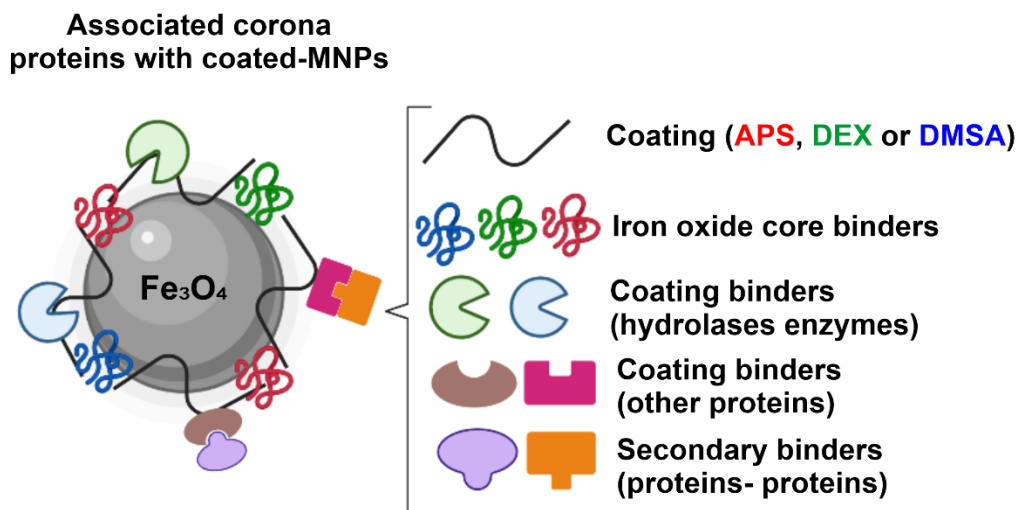


Figure 6. Schematic representation of the assembly of the PC of iron oxide coated-MNPs.

Evaluating the influence of the different coatings and their associated PCs on MNP internalization. Two cell lines were used to evaluate the impact of the PC on MNP cellular uptake: the mouse RAW 264.7 macrophage cell line and the mouse Pan 02 pancreatic tumor cell line (see Figure S6: Viability of RAW 264.7 macrophages and Pan 02 tumor cells treated with different concentrations of APS-MNPs, DEX-MNPs and DMSA-MNPs). In these studies we used specific chemical inhibitors to block some of the main internalization pathways: Chlorpromazine (CPZ), inhibitor of clathrin-mediated endocytosis that translocates clathrin and AP2 from the cell surface to intracellular endosomes; Amiloride (A), an inhibitor of macropinocytosis that impairs Na⁺/H⁺ exchanger activity; Cytochalasin D (C), an inhibitor of actin that acts by inducing actin cytoskeleton depolymerization; and Filipin III (F), an inhibitor of caveolae-dependent endocytosis that binds to cholesterol in the membrane (Figure 7a). Cells were cultured in DMEM with 10% FBS for 24 h and then treated with each inhibitor for 2 h before (see Figure S7: Viability of RAW 264.7 macrophages and Pan 02 tumor cells treated with different concentrations of endocytosis inhibitors as measured with a PrestoBlue assay), prior to their exposure for another 24 h to 125 µg

Fe/ml of the MNPs (APS-, DEX- or DMSA-MNPs) to allow their uptake. The number of MNPs internalized by cells was evaluated using an iron quantification assay (ICP-OES) and expressed relative to the maximum internalization measured as the iron content of cells incubated with MNPs but not treated with inhibitors. The basal iron content of the cells was measured in cells not treated with an inhibitor and not exposed to MNPs.

It is well known that NPs are mainly internalized through endocytosis³⁰, and that the NPs enveloped in the cell's membrane invaginations are then transported to specialized inner compartments. Depending on the cell type, endocytosis can be divided into phagocytosis and pinocytosis, and pinocytosis is then further classified into three main pathways: clathrin-mediated endocytosis, caveolae-mediated endocytosis and macropinocytosis. Larger NPs (> 500 nm) are mainly internalized by phagocytosis and macropinocytosis, while smaller ones use receptor-mediated mechanisms (<200 nm)¹³.

Quantification of RAW 264.7 cell iron concentrations indicated that APS-MNPs were internalized through all of the endocytic pathways: receptor-dependent endocytosis, endocytosis mediated by clathrin and caveolae, and macropinocytosis. DEX-MNPs were mainly internalized by caveolae-mediated endocytosis, while DMSA-MNPs were internalized mainly by clathrin- and caveolae-mediated endocytosis (Figure 7b). In the case of the Pan 02 tumor cell line, iron quantification indicated that APS-MNPs were mainly internalized by macropinocytosis, while DEX-MNPs were mainly internalized by clathrin- and caveolae-mediated endocytosis. In contrast to the macrophage cell line, Pan 02 appeared to take up the DMSA-MNPs through all the endocytic pathways (Figure 7c).

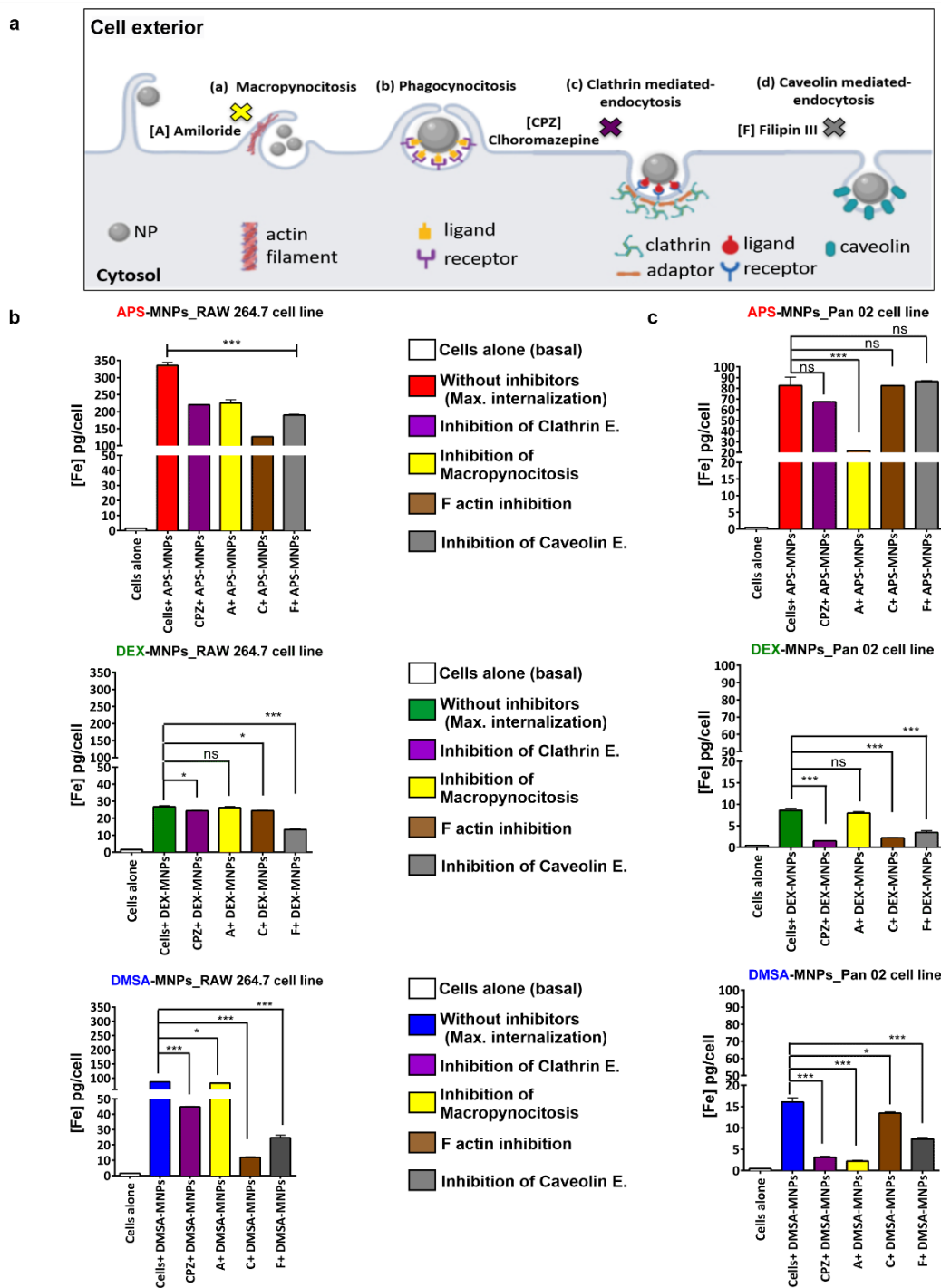


Figure 7. How the different coatings and the PCs formed on them influence MNP internalization. (a) Scheme of the inhibition of the different internalization pathways of MNPs. (b) Assay of endocytic pathways for differently coated MNPs (APS-, DEX- and DMSA-MNPs) in RAW 264.7 and (c) Pan 02 cells. Two-way analysis of variance (ANOVA) and Tukey's multiple comparison tests was performed for the different groups of iron concentration after the inhibition of uptake. Asterisks indicate samples showing statistically significant differences in iron concentration (ns - no significant differences): * $p < 0.05$, ** $p < 0.01$ and *** $p < 0.001$.

Amiloride caused the strongest reduction in APS-MNP uptake in both cell lines, suggesting that macropinocytosis was the main mechanism of internalization. By contrast, Chlorpromazine and Filipin III exerted the strongest influence on the DEX- and DMSA-MNP internalization, indicative of the active involvement of receptor-mediated mechanisms and specifically, caveolae-mediated (DEX-MNPs) or clathrin- and caveolae-mediated endocytosis (DMSA-MNPs: for similar results with other inhibitors of caveolae-mediated endocytosis see Supporting Materials and Methods, Supporting Results and Discussion, and Figure S8).

Actin plays a prominent role in macropinocytosis, mediating the formation of membrane ruffles⁴³, although it is also involved in other mechanisms like clathrin-mediated endocytosis. Receptor-mediated endocytosis was affected when these cells were treated with Cytochalasin D, mainly clathrin-mediated endocytosis. While the cytoskeleton is thought to be involved in the internalization of the MNPs via macropinocytosis, no correlation was evident between the inhibition of actin polymerization and the decrease of the MNP internalization by macropinocytosis (Figure 7b, c).

Considering that the corona protein composition and the relative abundance of proteins for the three types of coated MNPs was similar, we would have expected the same mechanisms of internalization to be at play if cell uptake was mainly dictated by the PC. However, the opposite effect was noted and indeed, both the size and shape of the NPs is thought to influence their internalization^{13, 30, 44}. As such, larger NPs were mainly internalized by phagocytosis and macropinocytosis, while smaller NPs were internalized by clathrin- or caveolae-mediated endocytosis⁴⁴. Similarly, the APS-MNPs that had the largest hydrodynamic size after incubation in 10 % FBS were internalized

mainly through macropinocytosis, whereas the significantly smaller DMSA- and DEX-MNPs entered cells through other mechanisms, as their uptake was barely affected by Amiloride, the inhibitor of macropinocytosis¹⁹. Inhibiting caveolae-mediated endocytosis in HUVEC cells reduced the internalization of small NPs (20 and 40 nm) by 80%, regardless of their coating, while the internalization of larger NPs (100 nm and 200 nm) was only reduced by 36%⁴⁵. Therefore, caveolae-mediated endocytosis depends more on size than on NP coating, although the PC composition on each coating was not analyzed.

Small gold-NPs (Au-NPs) (5 nm, 20 nm) were taken up via caveolae-mediated endocytosis, while larger Au-NPs (50 nm) were internalized via clathrin-mediated endocytosis or macropinocytosis⁴⁶. This difference appeared to be related to the PC associated with small Au-NPs, which inhibits caveolae-mediated endocytosis and therefore dampens NP uptake. Nevertheless, the PC disrupts the scavenger-receptor interaction of larger Au-NPs and thus, it inhibits caveolae-mediated endocytosis and promotes recognition by the clathrin-receptor. In essence, the PC exhibits a stronger inhibitory effect on caveolae-mediated endocytosis of Au-NPs as the nanoparticle size increases. The predominant uptake pathways of relatively small NPs (in terms of hydrodynamic size) are clathrin- and caveolae-mediated endocytosis^{45, 46}. Similarly, here caveolae- and clathrin-mediated endocytosis was that mainly involved in the uptake of the smaller NPs (DEX-MNPs, 109 nm and DMSA-MNPs, 83 nm) by both RAW 264.7 and Pan 02 cell lines. However, APS-MNPs were mainly internalized by macropinocytosis, most likely due to their large hydrodynamic size and the considerable size of the corona inhibiting the caveolae-mediated pathway.

Importantly, we didn't note a differential enrichment of proteins like opsonins (immunoglobulins of the IgG isotype and components of the complement system like

C3b, iC3b or C4b) that can influence internalization by interacting with cell membrane receptors. A high abundance of immunoglobulins in the PC is necessary and sufficient for binding to the Fc receptor, which could induce the uptake of NPs into macrophages⁴⁷. Here, the APS-MNPs were those best internalized by macrophages, which could be directly related to the size of the associated corona that was the largest in this case (Figure 7b). Although we cannot rule out the interaction of some of the PC-derived proteins with the cell membrane receptors, our data suggest that the MNP layer mainly governs the internalization process by influencing PC thickness rather than its composition. Indeed, the coating was shown to influence internalization previously¹⁸.

Surface charge appears to be an important factor regulating NP uptake by cells⁴⁸ and in RAW 264.7 cells, iron oxide NPs with a very positive charge are taken up faster than PEG-coated NPs with an almost neutral charge⁴⁹. This is consistent with our observations, as APS-MNPs were internalized 12 times more rapidly than DEX-MNPs in RAW 264.7 cells. Indeed, iron oxide NPs with a positive charge were found in a higher concentration intracellularly than negatively charged ones⁵⁰. PEI-coated NPs (positive charge) are taken up through clathrin- and caveolae-mediated endocytosis due to their interaction with the TLR4 receptor on RAW 264.7 cells^{51,52}. Here, APS-MNPs have a similar positive superficial charge to PEI-coated NPs, and they were largely internalized by macropinocytosis due to their hydrodynamic size. Nonetheless, clathrin- and caveolae-mediated endocytosis were partly involved in their uptake. APS-coated NPs were internalized by phagocytosis in human lung cancer SPC-A1 cells⁵³ and DEX-coated NPs (Ferumoxides and Carboxydextran-coated NPs) were seen to be mainly internalized by human macrophage cells^{54,55} via clathrin-mediated endocytosis. We found DEX-MNPs mainly used caveolae-mediated endocytosis for uptake by RAW 264.7 cells, whereas clathrin-mediated endocytosis was as significant as caveolae-

mediated endocytosis in Pan 02 cells, which supports the findings described previously¹⁸.

TEM images were analyzed to corroborate the pathway by which each MNP was internalized in the conditions described above. The simplest way to identify endocytic pathways is through the ultrastructural morphology of the endocytotic intermediates at the plasma membrane. As such, we detected three structures typical of endocytotic pathways: clathrin-coated pits (associated with clathrin-mediated endocytosis), flask-shaped structures without an electron-dense coat (associated with caveolae-mediated endocytosis) and larger macropinocytic vesicles (macropinosomes) that identify macropinocytosis⁵⁶. These structures were identified during the uptake of the different MNPs. In the RAW 264.7 cells, clathrin-coated pits and macropinosomes were detected during APS-MNP internalization, indicating that clathrin-mediated endocytosis and macropinocytosis were activated. DEX-MNPs uptake was associated with flask-shaped structures, suggesting the activation of the caveolae-mediated endocytosis, whereas two distinguishable invaginations were observed in the membrane during DMSA-MNP internalization, clathrin-coated pits and flask-shaped structures indicative of clathrin- and caveolae-mediated endocytosis (Figure 8a, b).

In pancreatic Pan 02 tumor cells, only macropinosomes were observed in the cell membrane following exposure to APS-MNPs, suggesting their uptake by macropinocytosis. However, both clathrin-coated pits and flask-shaped structures were identified when DMSA-MNP internalization was analyzed, suggesting the prevalence of clathrin- and caveolae-mediated endocytosis. By contrast, the DEX-MNPs only appeared to enter the cells through clathrin-coated pit structures, a *bona fide* indication of clathrin-mediated endocytosis. However, caveolae-mediated endocytosis of DEX-

MNPs also appeared to be active during the functional analysis when the endocytosis pathways were inhibited (Figure 8c, d).

Despite the similar PC compositions, there were clear differences in the internalization pathways for each type of MNP, suggesting that the coating largely dictates the internalization pathway rather than the PC composition. However, a certain contribution of the corona and an influence of MNP aggregation cannot be completely ruled out, not least because the hydrodynamic size sometimes determines the internalization pathway used, as noted for the APS-MNPs. Nevertheless, the prevailing internalization pathway in all cases was macropinocytosis, which is evidence of a direct relationship between the MNP's hydrodynamic size and the internalization pathway.

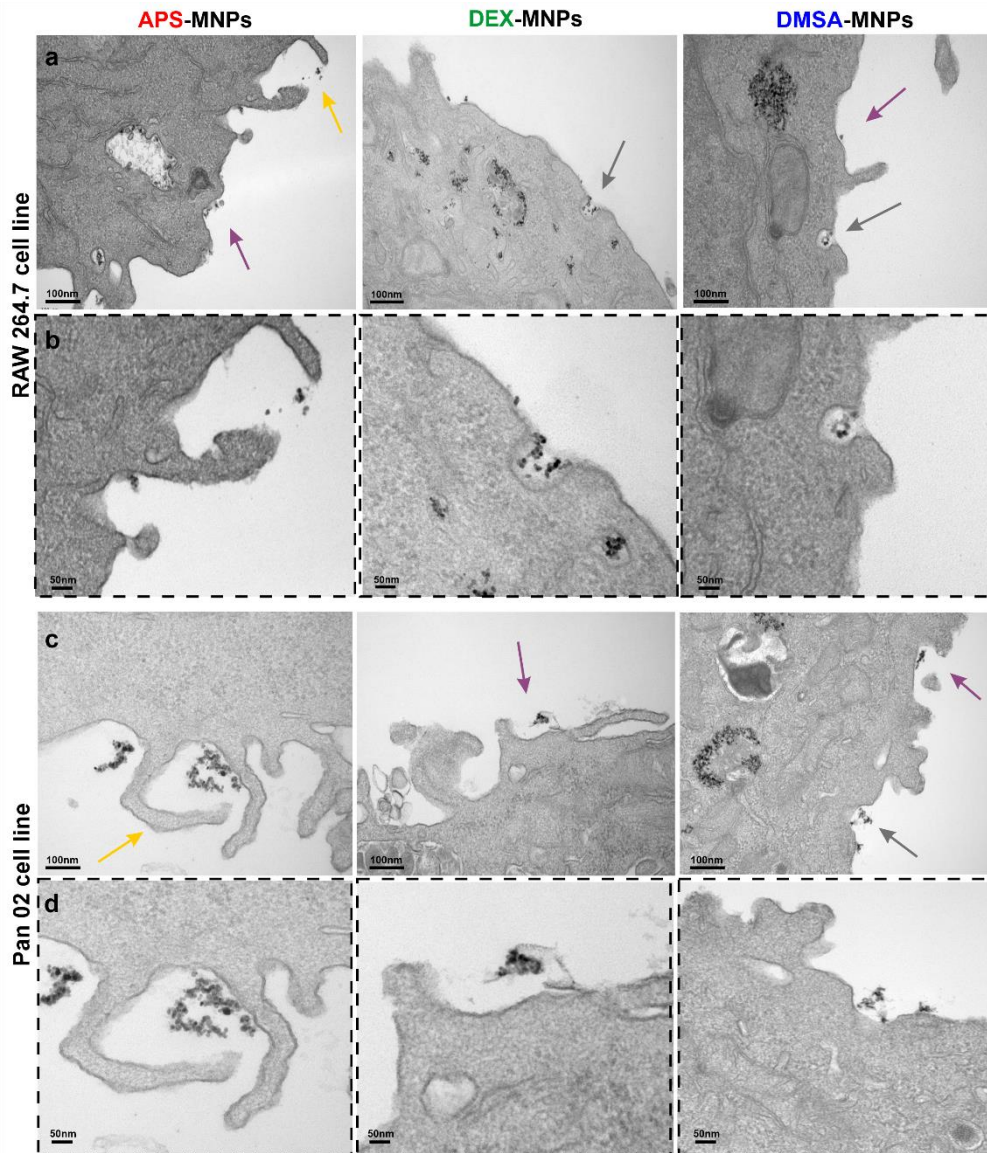


Figure 8. TEM analysis of the typical membrane structures associated with MNP internalization in RAW 264.7 and Pan 02 cells. (a, c) TEM images of MNP internalization. (b, d) Detailed images highlighting the MNP internalization pathways (magnification 150×200). Colored arrows indicate the structures associated with the specific mechanisms of MNP internalization: purple, clathrin-mediated endocytosis (clathrin-coated pits); gray, caveolae-mediated endocytosis (flask-shaped structures); and yellow, macropinocytosis (macropinosomes). Scale bar: 50 and 100 nm.

Together, we conclude that the main internalization pathway for APS-MNPs is macropinocytosis, whereas caveolae-mediated endocytosis prevails for DEX-MNPs and receptor-mediated endocytosis (clathrin- and caveolae-mediated) governs the internalization of DMSA-MNPs. The internalization of APS-MNPs, with their positive

surface charge, is influenced by the increase in hydrodynamic size provoked by the association of the PC.

Regarding the influence that the PC may have on cellular processes, there are two main hypothesis: one that states that the PC is a key factor in the interaction between cells and MNPs^{16, 57}; and another recognizing the importance of the PC in the stability of the MNPs^{34, 58}, whereby the physicochemical properties of the nanomaterials (e.g. size, charge and coating) are decisive factors dictating these interactions⁵⁹⁻⁶¹. The results obtained here suggest that physicochemical parameters have a strong influence on MNP uptake and that the PC does not overshadow this effect. Some of the differences observed experimentally support both hypotheses, which could depend on the experimental approach used⁶² and the complexity of the interactions of the system presented by the nanobio interfaces, the cell types and the MNPs^{48, 63}.

Protein corona degradation kinetics after cell internalization. Once the MNPs are internalized by cells, we assessed the kinetics of PC degradation by two experimental approaches. In the first, a fluorescent-labeled PC was generated by labeling FBS proteins with the fluorescent dye Alexa Fluor 488 (1:10, for 1h at RT) and the reduction in fluorescence intensity over time was tracked to follow PC degradation. APS- or DMSA-MNPs were then incubated in DMEM containing 10% fluorescently labeled FBS for 24 h to generate PCs of fluorescent proteins from the labeled serum. Finally, RAW 264.7 or Pan 02 cells were incubated for 24 and 48 h with these APS- or DMSA-MNPs with fluorescent coronas (125 µg/ml) in a final volume of 1ml (Figure 9a). APS- and DMSA-MNPs were chosen for this experiment given the hydrodynamic size of the corona and their rate of internalization. As APS-MNPs formed the largest coronas and DMSA-MNPs the smallest (Figure 2b), the influence of size of the corona on

degradation could be assessed. In addition, these two types of coated NPs were those with the higher internalization rates, enabling us to better follow the labeled corona inside the cells. DEX-MNPs were poorly internalized in the cell lines used here (Figure 7b, c and Figure S9).

In both cell lines, many green dots were seen in the cytoplasm after a 24 h incubation of the APS- or DMSA-MNPs with fluorescent PCs, largely co-localizing with lysosomes labeled with LysoTracker-red (Figure 9b, c). Interestingly, a 5- and 2-fold reduction in fluorescence intensity was observed after 48 h in the APS-MNP treated RAW 264.7 and Pan 02 cells, respectively. Likewise, we noted a 4- and 2-fold reduction after 48 h in the DMSA-MNP treated RAW 264.7 and Pan 02 cells, respectively (Figure 9d, e). As expected, we also found that the RAW 264.7 macrophages degraded the PC at a higher rate than the tumor cells Pan 02 (Figure 9d, e), mirroring several *in vivo* degradation studies where internalized NPs were mainly degraded by macrophages from the liver and spleen^{43, 44}. Apart from the cell type, the superficial charge of the NPs can influence their degradation, as NPs with negative superficial charges were first localized within endosomes and then lysosomes, while positively charged NPs seem to accumulate rapidly in lysosomes^{19, 50}. When fluorescently labeled serum proteins were previously used to form a fluorescent PC on positively charged PEI-coated NPs, these were seen to localize to lysosomes after internalization, where they were degraded⁶⁴. Here, anionic (DMSA-MNPs) and cationic (APS-MNPs) NPs, with their respective coronas, were degraded in lysosomes in both cell lines (Figure 9b, c).

In summary, measuring AlexaFluor 488 fluorescence intensity highlighted the rapid disappearance of the fluorescent signal arising from labeled coronas 24 h after MNPs were taken up by cells, suggesting the fast degradation of the PC after MNP internalization.

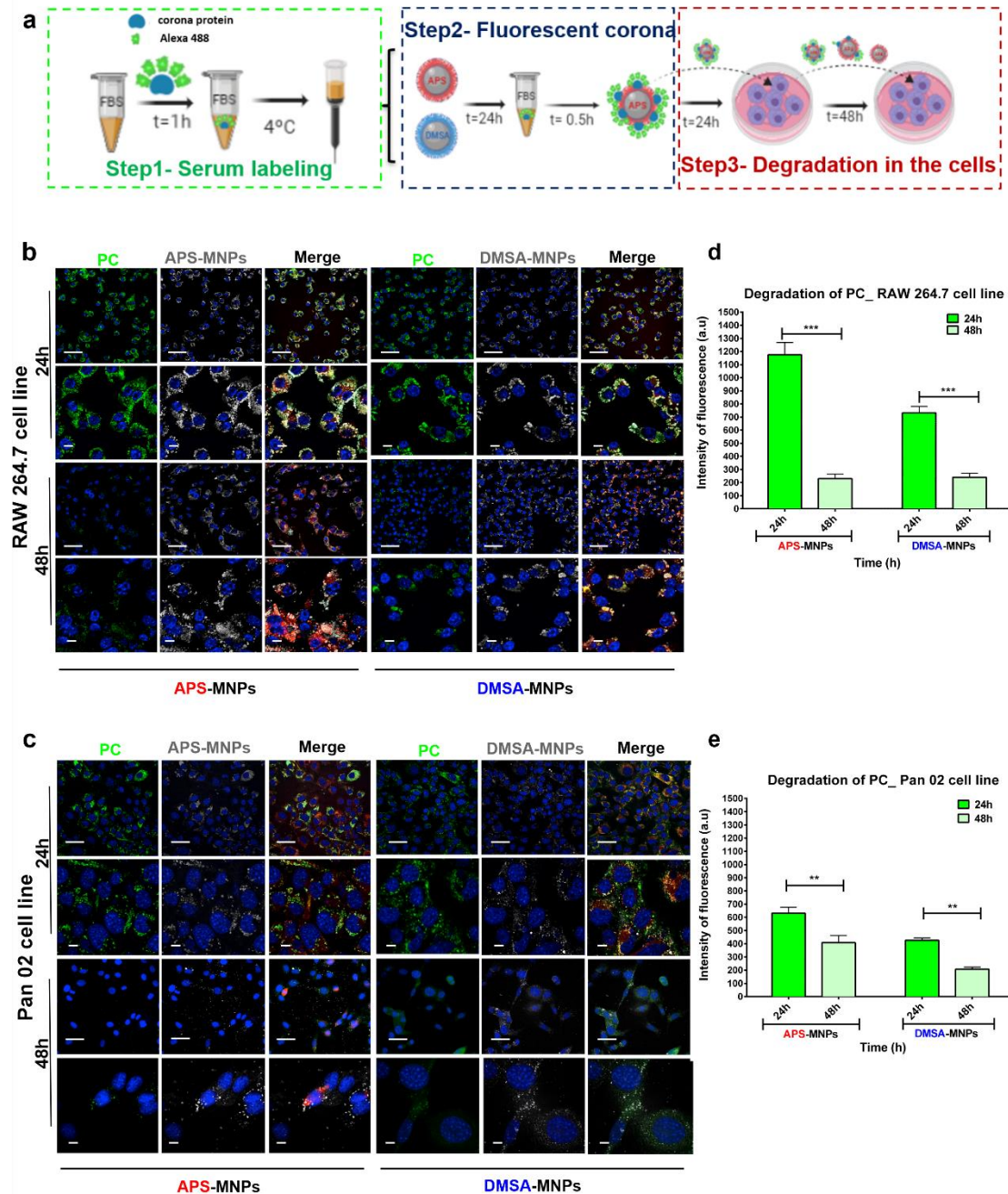


Figure 9. Analysis of Alexa 488 labeled PC degradation after internalization by RAW 264.7 or Pan 02 cells. (a) Scheme representing the fluorescent labeling of serum proteins, the formation of a labeled fluorescent corona on coated-MNPs, and MNP uptake. (b, c) Confocal microscopy images of internalized MNPs with Alexa 488 labeled coronas in RAW 264.7 and Pan 02 cells at 24 and 48 h: lysosomes, LysoTracker-red; PC, Alexa 488-green; nuclei, DAPI-blue; and MNPs, gray. Scale bar: 10 μ m, 63X magnification and zoom 3. (d) Quantification of Alexa 488-fluorophore intensity associated with APS-MNPs or DMSA-MNPs PCs incubated for 24 and 48 h on RAW 264.7 cells. (e) Quantification of the Alexa 488 fluorophore intensity associated with APS-MNPs or DMSA-MNPs PCs incubated for 24 and 48 h in Pan 02 cells. Data (mean \pm SD) are representative of three independent experiments and the asterisks indicate samples showing statistically significant differences: * $p < 0.05$, ** $p < 0.01$, *** $p < 0.001$ (One-way analysis of variance -ANOVA, Student's t-test).

It cannot be ruled out that the AlexaFluor 488 fluorophore was degraded faster than the labeled corona proteins and thus, we used a more quantitative strategy by generating a PC on coated-MNPs from only chicken ovalbumin (OVA). As OVA had a higher affinity for APS-MNPs given their electroaffinity, only these MNPs were studied. This approach allowed us to follow OVA degradation by quantifying the main peptides produced over time using targeted proteomics. APS-MNPs were incubated with fluorescent-OVA to generate a PC formed exclusively by OVA and its degradation was analyzed in RAW 264.7 cells that had a faster degradation rate in the experiments with FBS. Moreover, the protocol to form an OVA corona on APS-MNPs (henceforth APS-MNPs-OVAC) was optimized (see Supporting Materials and Methods, Figure S10).

The main OVA peptides were identified from purified OVA and APS-MNPs-OVAC (see Supporting Materials and Methods and Supporting Results and Discussion, Figure S11), and 45 peptides were detected in the purified OVA sample, while only 3 were detected in the pool of proteins extracted from APS-MNPs-OVAC (Figure S11b, c). Hence, the digestion of the OVA coupled to the APS-MNPs seems to be more inefficient than the digestion of purified OVA. The fragmentation spectra of each peptide identified were subsequently analyzed to select the transitions that would later be studied by directed proteomics (Figure S11d). To follow corona degradation, RAW 264.7 cells were incubated with APS-MNPs-OVAC (50 $\mu\text{g}/\text{ml}$) for 24 h (conditions determined in studies detailed in the Supporting Information, Figure S12) and the greatest compaction of APS-MNPs-OVAC in lysosomes (observed by confocal microscopy) occurred 24 h after their uptake by RAW 264.7 cells. Thus, cells were lysed 24, 48 and 72 h after they were initially exposed to the MNPs (time 0), processed and the selected OVA peptides in the lysates were detected by directed proteomics. The limits of detection were evaluated by directed proteomics on serial dilutions of a

purified OVA, verifying that the peptides could be detected at a very low concentration (2 ng). This approach was also used to identify the elution time and the composition of the peaks of each peptide (one peak per transition), and the results showed that these peaks were increasingly diffuse as the OVA concentration diminished, ceasing to be detected below 4 ng. To identify a specific peptide in a sample, the peak must be observed at the same elution time and the relationship between the peak intensity of the different transitions must be consistent (in Figure 10 the most intense peaks were y3, then y5, y4 and finally, y6).

The detection of the DEDTQAMPFR peptide at 24, 48 and 72h was examined (Figure 10). A peak at an elution time close to that obtained with the purified OVA sample was observed, although the slight differences mean we cannot ensure this corresponds to the OVA peptide. The elution peak from purified OVA was observed at 19.9 minutes whereas it was delayed until the 20.5 minutes in the case of APS-MNPs-OVAC (Figure 10b), consistent with the transitions of the peptide for the degradation times analyzed. This change in the elution time could be explained by the increased complexity of the peptide bound to the coating, which could trigger distinct digestion processes.

In the APS-MNPs-OVAC sample we observed a signal in the y3 and y5 transitions 24 h after internalization, whereas no peak was appreciated in the expected 19-21 minutes range after 72 h, which we believe reflects the complete degradation of OVA. Hence, after this analysis we concluded that the OVA corona formed on APS-MNPs was completely degraded between 24 to 72 h after internalization, 24 to 48h after being compacted in lysosomes.

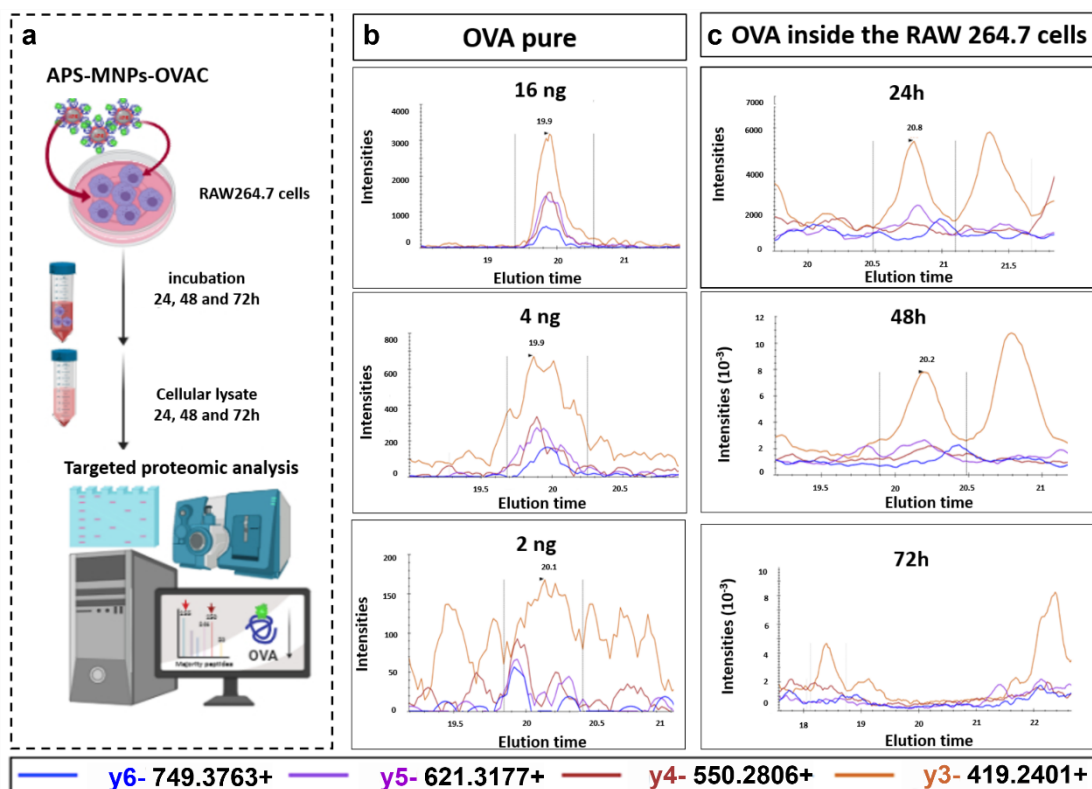


Figure 10. Analysis of OVA-PC degradation on APS-MNPs, quantifying the main OVA peptides by targeted proteomics. (a) Scheme of the experimental strategy used to follow the degradation of an OVA corona on APS-MNPs after its internalization by RAW 264.7 by directed proteomics analysis. (b) Detection of the DEDTQAMPFR peptide in the purified OVA sample at different dilutions. A peak formed by 4 transitions (y3, y5, y4, y6 in order of peak intensity) was observed at an elution time of 19.9 minutes. (c) Detection of the DEDTQAMPFR peptide in lysates from RAW 264.7 incubated with APS-MNPs-OVAC obtained at different degradation time points. In these samples the elution time is slightly offset, which could be due to the presence of the MNPs. The scale of the graphs had to be adjusted to correctly show the transition peaks.

Similar PC degradation times have been reported elsewhere using NPs with a fluorescent-labeled PC¹⁶, with the degradation of serum PC associated with a NP (at least 16h) significantly slower than that of free serum proteins (a maximum of 6 h once internalized). Here, we found that similar fluorescent PC NPs were significantly but not completely extinguished 24 h after NPs were internalized (Figure 9d, e), with complete degradation of the corona observed 72 h after internalization in targeted proteomics experiment. Using a fluorophore labeled OVA-PC with APS-MNPs, complete degradation was confirmed when no OVA peptides were detected (Figure 10c).

There appears to be a direct correlation between the *in vitro* composition of the PC and its biodistribution *in vivo*¹⁴, and NP degradation *in vitro* was thought to depend on two factors: the coating, which influences the degradation rate; and the PC, which protects the core from the acidic conditions of the medium. Using an *in vitro* degradation assay, glucose-coated NPs that form a larger PC than PEG-coated NPs when incubated in DMEM with 10% FBS, were degraded faster than PEG-coated NPs that form a smaller PC¹⁴. We observed a similar situation between APS-MNPs, which formed a 1480 nm PC that was degraded faster than the 140 nm corona formed on DMSA-MNPs. This might suggest that a correlation possibly exists between the number of proteins forming the associated corona of a NP and its degradation rate.

CONCLUSIONS

In summary, after analyzing PC formation on APS-MNPs, DMSA-MNPs or DEX-MNPs incubated in DMEM with 10% FBS for 72 h, we conclude that the hydrodynamic size reaches a maximum after 5-10 h, thereafter decreasing until a stable size is reached 24 h after incubation. Subsequently, the hydrodynamic size of the corona remains stable without significant changes. A proteomic analysis of the PC composition on MNPs with APS, DEX and DMSA coatings showed an enrichment of proteins with affinity for divalent ions, which was most evident in DEX-MNPs due to a defective coating. This suggests that the iron oxide core could influence the formation of the PC to a similar extent as the polymeric coating.

A temporal analysis of the integrity of the polymeric MNP coatings after coming into contact with medium containing serum showed a change in the IR spectra that was compatible with the degradation of the coating. Together with the detection of proteins with enzymatic activity in the pool of proteins that form the coronas, it appears that the

corona could degrade the coatings as it forms, most notably in the cases of APS- and DEX-MNPs. Indeed, 20% of these proteins seemed to be hydrolases.

Clear differences in the internalization pathways were observed for each type of MNP, despite the similar compositions of their associated PC. APS-MNPs were internalized via macropinocytosis, DEX-MNPs via caveolae-mediated endocytosis and DMSA-MNPs via receptor-mediated endocytosis (both clathrin- and caveolae-mediated). This indicated that the coating mainly dictates the pathway of internalization used. However, the increase in the hydrodynamic size of the MNP caused by corona formation also influences the internalization pathway used by APS-MNPs.

Two different approaches to study the degradation process of the PC, measurement of a fluorescent labeled PC with and targeted proteomic analysis of an ovalbumin engineered PC, showed that once internalized the MNPs concentrate in lysosomes and are rapidly degraded.

MATERIALS AND METHODS

Reagents used to synthesize and characterize the MNP iron oxide cores. FeCl_2 ($\geq 99.0\%$, Sigma-Aldrich), FeCl_3 (27%, VWR International), NH_4OH (25%, Fluka), HNO_3 ($< 65.0\%$, Sigma-Aldrich), $\text{Fe}(\text{NO}_3)_3$ ($> 98.0\%$, Sigma-Aldrich) and methanol ($> 98.0\%$, Sigma-Aldrich). APS, DEX (6kDa) and DMSA were purchased from (Sigma-Aldrich, $> 98\%$).

Cells, Culture Medium and Biological Reagents. The biological reagents for this work were acquired from the following providers: RAW 264.7 cells (ATCC: TIB-71) from the American Type Culture Collection; Pan 02 cells (RRID: CVCL-D627) from NCI-DTP; Dulbecco's modified Eagle medium (basic, 1X), FBS, L-glutamine, penicillin-streptomycin and sodium pyruvate from Biowest; PrestoBlue Cell Viability

Reagent, Alexa Fluor 488 5-SDP ester, Alexa Fluor 488 conjugate and ovalbumin from Invitrogen; LysoTracker, DAPI and Prolong Gold from Thermofisher; Chlorpromazine (C8138), Amiloride (A0370000), Cytochalasin D (C8273) and Filipin III (F4767) from Sigma-Aldrich.

Synthesis of MNP iron oxide cores. The iron oxide cores of the MNPs used were synthesized following the Massart co-precipitation method, according to previously described protocols²⁵. Briefly, a mixture of 445 ml of $\text{FeCl}_3 \cdot 6\text{H}_2\text{O}$ (0.09 mol) and $\text{FeCl}_2 \cdot 4\text{H}_2\text{O}$ (0.054 mol) was slowly added to 75 ml of NH_4OH (25%) with vigorous stirring, and heated to 90 °C for 90 minutes to prepare nanoparticles (NPs) approximately 12 nm in diameter. The sample was then washed three times with distilled water by magnetic decantation and after core synthesis, and a standard protocol was used to oxidize magnetite to maghemite ($\gamma\text{-Fe}_2\text{O}_3$) and activate the surface⁶⁵. The MNPs were then cooled to room temperature (RT) and the supernatant was substituted by 300 ml of HNO_3 (2 M) by magnetic decantation and stirred for 15 min. Finally, the NPs were washed three times with acetone and dispersed in distilled water. A rotary evaporator was used to remove any acetone waste and concentrate the sample.

MNP surface coating. Iron oxide cores were coated with 3-aminopropyl-triethoxysilane, dextran 6 kDa and dimercaptosuccinic acid, according to previously described procedures⁶⁶. Briefly, for APS coating (APS-MNPs), 1.17 ml (0.005 mol) of APS was added to a mixture of 10 ml of the iron oxide cores (Fe_2O_3 , 28 g/l) and 10 ml of methanol, and stirred vigorously for 12-16 h. The methanol was evaporated from the mixture using a rotary evaporator, the sample was washed three times with a mixture of acetone/water (70/30) and then re-dispersed in 10 ml of distilled water. The pH was decreased to 3 and the sample was sonicated for 1 h. Finally, the pH was adjusted to 7 and sonicated for 10 min. For DEX coating (DEX-MNPs), the dispersed iron oxide core

(600 mg of Fe₂O₃ in 4.8 ml NaOH [0.8 M]) was added dropwise to a solution of 600 mg of dextran in 7.5 ml NaOH (0.5 M) under sonication. The mixture was sonicated for 6 h with refrigeration and after coating, this suspension was dialyzed for 3 days and the pH was adjusted to 7. Finally, for DMSA coating (DMSA-MNPs), 14.7 mg (0.08 mmol) of DMSA was added to a 30 ml suspension of the iron oxide cores (0.05 M) with stirring at pH 3. The pH was then increased to 11 by adding KOH and the sample was sonicated for 20 min. Finally, this suspension was dialyzed for two days and the pH was adjusted to 7.

MNP characterization. Particle size and shape was determined by TEM. A drop of the NP suspension was placed on a carbon-coated copper grid and the solvent was allowed to evaporate at RT. Images were captured on a 100 keV JEOL-JEM 1010 microscope equipped with a Gatan Orius 200 SC digital camera. The TEM images were analyzed using ImageJ software (NIH, USA) to determine the MNPs' size, shape and distribution. After the coating process, the MNPs were analyzed in water to determine their hydrodynamic size and Z-potential. Then, DLS for colloidal characterization was carried out using a NanoSizer ZS (Malvern). The amount and composition of the coating was determined by FTIR. Samples were prepared by diluting iron oxide powder (2% wt) in KBr and compressing the mixture into a pellet. The spectra selected were between 4000-400 cm⁻¹ in a Bruker IFS 66 V-S spectrometer and a Nicolet FT-IR 20SXC (Thermo Scientific, USA). Simultaneous TG analysis and differential thermal analysis (DTA) was performed on a Seiko TG/DTA 320U device. For these analyses, samples were heated from RT to 900 °C at 10 °C/min with a continuous air supply of 100 ml/min. The iron concentration was measured with an Optima 2100 DV inductively coupled plasma optical emission spectrometer (ICP-OES; PerkinElmer). The crystal structure of the sample was identified by X-Ray powder diffraction performed in a

Bruker D8 Advance diffractometer (with Cu K α radiation, scan angle (10°-70°). The patterns were collected within 10° and 90° in 2 θ . For the magnetic characterization, liquid samples were frozen and dried overnight in a LyoQuest freeze dryer (Telstar, Spain). The resulting solid sample was compacted into gelatin capsules for magnetic characterization. Hysteresis loops with a maximum field of 5 T were measured in a Vibrating Sample Magnetometer (MLVSM9, MagLab 9T, Oxford Instruments, UK).

Cell culture. The murine Pan 02 and RAW 264.7 cell lines were cultured in DMEM supplemented with 10% (v/v) FBS, 100 U/ml penicillin, 100 U/ml streptomycin, 2 mM L-glutamine, 1 mM non-essential amino acids and sodium pyruvate (all from Biowest). The cells were maintained under standard culture conditions (37 °C, 5% CO₂ and 90% relative humidity).

Study of corona formation. To study the process of PC formation, MNPs (APS-MNPs, DEX-MNPs or DMSA-MNPs: 125 μ g Fe/ml) were incubated in DMEM supplemented with a 10% FBS at 37 °C for different times (0, 1, 3, 5, 10, 24, 48, or 72 h). In some of the samples, loosely-bound proteins were separated from aliquots of the MNPs incubated with FBS. As such, the MNPs were centrifuged at 12,000 rpm for 5 min to separate the MNPs from the medium containing 10% FBS, and they were then washed twice with 1 ml of PBS (pH 7.4), recovered by centrifugation for 30 minutes at 15,000 rpm (Supernatants S1 and S2) and finally re-dispersed in PBS (final resuspension -FR). The hydrodynamic size of the unwashed MNPs incubated with FBS and the FR MNPs, was measured according to the protocol described above (“MNP characterization”).

To quantify the total amount of proteins attached to the MNPs and the proportion of proteins loosely or stably attached to MNPs, the supernatants from the washes with PBS (S1 + S2), and the FR were incubated with a protein extraction buffer containing:

Triton X-100, 1 mM EDTA, protease inhibitors 1 µg/ml leupeptin, 5 nM NaF, 1 mM sodium orthovanadate, 1 mM phenylmethylsulfonyl fluoride (PMSF), 0.5 mM EDTA, 1 µg/ml aprotinin and 1 µg/ml okadaic acid. Subsequently, the total protein concentration in the supernatants and FR was quantified using the BCA kit (ThermoFisher) and finally, the proportion of loosely and stably attached proteins was calculated according to the following formulae:

$$\% \text{Proteins loosely attached (S1 + S2)} = \frac{[S1 + S2]}{[\mu\text{g initial PC associated}]} * 100$$

$$\% \text{Proteins stably attached (FR)} = \frac{[FR]}{[\mu\text{g initial PC associated}]} * 100$$

$$[\mu\text{g initial PC associated}] = \mu\text{g of proteins in S1} + \mu\text{g of proteins in S2} + \mu\text{g of proteins in FR}$$

To analyze the changes in surface charge due to corona formation over time, the Z potential of the MNPs maintained in water and when incubated with DMEM plus 10% FBS was measured at pH 7 using the NanoSizer ZS (Malvern).

Proteomic characterization of the PC associated with the MNPs

Extraction of the PC associated with the MNPs. MNPs of each type (APS-MNPs, DEX-MNPs or DMSA-MNPs), corresponding to 0.125 mg of Fe, were incubated for 24 h at 37 °C with FBS at a final volume of 8 ml to allow the PC to form. The MNPs were then separated from the FBS-containing medium using a magnet, and they were washed with PBS and recovered by centrifugation three times. To extract the proteins that form the corona from the MNP's surface, the MNPs were resuspended in the protein extraction buffer indicated above and finally, the total protein concentration was quantified in each extract using the BCA kit (ThermoFisher).

Trypsin digestion. PC protein extracts were washed sequentially for 30 min with different buffers: (a) 50 mM HEPES, 0.1% OGP [pH 7]; (b) 100 mM NaAc, 0.1% OGP [pH 5]. Each sample was shaken in a laboratory tube rotator with 2 ml of the

corresponding buffer solution for 30 min and then centrifuged for 10 min at 4 °C in a microcentrifuge. The supernatant was collected and stored at -80 °C until analysis. Each sample (10 µg) was individually loaded onto a 12% SDS-PAGE gel and after a short (10-15 min) separation, each sample was cut in 3-4 slices and these were trypsin digested using an automatic robot Proteineer (Bruker, Bremen, Germany). In all cases, digestion was performed according to Schevchenko *et al.*⁶⁷, first washing the gel plugs with 50 mM ammonium bicarbonate and reducing the samples with 10 mM DTT. Alkylation was carried out with 55 mM IAA at RT before adding recombinant sequencing-grade trypsin (0.1 µg: Promega) and digesting the proteins at 37 °C for 18 h. Following digestion, the peptides were extracted, pooled, dried by speed-vac centrifugation and stored at -20 °C until needed.

LC-ESI-MSMS analysis and database searching. Nano LC ESI-MSMS analysis was performed using an Eksigent 1D-nanoHPLC coupled to a 5600TripleTOF QTOF mass spectrometer (Sciex, Framingham, MA, USA). The analytical column used was a silica-based reversed phase column: Waters nanoACQUITY UPLC, 75 µm × 15 cm, 1.7 µm particle size. The trap column was an Acclaim PepMap 100, 5 µm particle diameter, 100 Å pore size, switched on-line with the analytical column. The loading pump delivered a solution of 0.1% formic acid in 98% water/2% acetonitrile (Scharlab, Barcelona, Spain) at 3 µL/min. The nanopump provided a flow-rate of 250 nL/min and was operated under gradient elution conditions, using 0.1% formic acid (Fluka, Buchs, Switzerland) in water as mobile phase A, and 0.1% formic acid in 100% acetonitrile as mobile phase B. Gradient elution was performed according the following scheme: isocratic conditions of 96% A:4% B for five minutes, a linear increase to 40% B in 105 min, a linear increase to 95% B in two minutes, isocratic conditions of 95% B for five minutes and return to initial conditions in 10 min. The injection volume was 5 µL and

the LC system was coupled via a nanospray source to the mass spectrometer. Automatic data-dependent acquisition using dynamic exclusion allowed both full scan (m/z 350-1250) MS spectra followed by tandem MS CID spectra of the 25 most abundant ions to be obtained. The acquisition time was 250 ms and 100 ms for MS and MSMS spectra, respectively. All the data was acquired using information-dependent acquisition (IDA) mode with Analyst TF 1.7 software (AB SCIEX, USA).

Data analysis and statistics. MS/MS spectra were exported to mgf format using Peak View v1.2.0.3, combined and searched using Mascot Server 2.5.1, OMSSA 2.1.9, X!TANDEM 2013.02.01.1 and Myrimatch 2.2.140 against a composite target/decoy database built from 7932 *Bos Taurus* protein entries found at Uniprot Knowledgebase, together with commonly occurring contaminants. After recalibration of parent ion mass measurements using high-scoring X!TANDEM hits, search engines were configured to match potential peptide candidates with a mass error tolerance of 10 ppm and fragment ion tolerance of 0.02Da, allowing for up to two missed tryptic cleavage sites and isotope error (^{13}C) of 1, considering fixed MMTS modification of cysteine and variable oxidation of methionine, with pyroglutamic acid from glutamine or glutamic acid at the peptide N-terminus, and acetylation of the protein N-terminus. Score distribution models were used to compute peptide-spectrum match p-values⁶⁸, and spectra recovered by a $FDR \leq 0.01$ (peptide-level) filter were selected for quantitative analysis. Approximately 5% of the signals with the lowest quality were removed prior to further analysis. Differential regulation was measured using linear models⁶⁹, and statistical significance was measured using q-values (FDR). All analyses were conducted using software from Proteobotics (Madrid, Spain).

Analysis of MNP uptake by cells

Quantification of the iron uptake by ICP-OES. Cells were seeded in a 6-well plate at a density of 2×10^5 cells per well, and incubated for 24 h at 37 °C. APS-, DEX- or DMSA-MNPs (125 µg Fe/ml) were then added and incubated in the same culture conditions for another 24 h. Subsequently, the cells were washed three times with PBS to remove non-internalized NPs, harvested and counted in a Neubauer chamber. The samples were digested in HNO₃ (1 ml) and H₂O₂ (1 ml) for 1h at 90 °C, and the amount of iron per cell was measured by ICP-OES (Perkin Elmer-2400).

Analysis of MNP uptake and the subcellular localization of MNPs using transmission electron microscopy. For TEM microscopy, 2×10^6 cells were seeded on petri dishes for 24 h. After that, 125 µg Fe/ml of each MNP (APS, DEX or DMSA) was added to the cells and left for 24 h. Non-internalized NPs were removed by washing with PBS and the cells were then fixed at RT in 2 % glutaraldehyde, 1 % tannic acid in 0.4 M HEPES [pH 7.2]. The cells were washed and suspended in HEPES buffer, post-fixed with 1% osmium tetroxide (1 h) and 2% uranyl acetate (30 min; both at 4 °C), dehydrated with a series of acetone solutions and gradually infiltrated with Epon resin. The resin was allowed to polymerize (60 °C, 48 h) and ultrathin sections (60-70 nm) were obtained with a diamond knife mounted on a Leica EM UC6 ultramicrotome. Sections were supported on a formvar/carbon-coated gold grid and observed on a JEOL-1011 transmission electron microscope, acquiring images at different magnifications with a Gatan ES1000Ww camera.

Use of inhibitors to evaluate the contribution of different endocytotic pathways to MNP internalization. Cells (RAW 264.7 or Pan 02 cells) were seeded in a 6-well plate at a density of 2×10^5 cells per well (24 h, 37 °C) and they were then pre-treated for 2 h with different inhibitors of endocytosis: Chlorpromazine (5 µg/ml), inhibitor of clathrin-mediated endocytosis; Filipin III (0.25 µg/ml), inhibitor of caveolae-dependent

endocytosis; Amiloride (0.78 $\mu\text{g/ml}$), inhibitor of macropinocytosis process; or Cytochalasin D (5 $\mu\text{g/ml}$), inhibitor of large F-actin-coated vesicle formation. To determine the optimal concentration of each inhibitor, a cell viability analysis was carried out for both cell types (see Supporting Materials and Methods and Figure S7). The cells pre-treated with the inhibitors of endocytosis were then incubated with MNPs (APS-, DEX- or DMSA-MNPs: 125 $\mu\text{g/ml}$) for 24 h in the presence of the same dose of those inhibitors and the total amount of internalized iron was quantified by ICP-OES. Maximum internalization was quantified with cells not exposed to the inhibitors of endocytosis. TEM images were used to analyze the subcellular localization of MNPs and to visualize the cellular structures that identify the pathways by which NPs were internalized (Figure 7a).

Analysis of polymeric coating degradation by corona proteins. To evaluate whether the proteins that form the MNP corona could induce degradation of MNP coatings after PC formation, APS-, DEX- or DMSA-MNPs (125 $\mu\text{g/ml}$) were incubated for 24 h at 37 °C in a final volume of 8 ml DMEM containing 10% FBS to allow PC formation and stabilization. The MNPs were then separated from the medium using magnets and washed three times in PBS buffer containing 5M NaCl (high salt buffer) to detach as many of the corona-forming proteins as possible from the MNP coating. Finally, the washed MNPs were lyophilized, and the IR spectra of the MNP coatings before and after incubation in the medium containing serum were analyzed as described above (see MNP characterization). To evaluate the degradation of the polymeric coating of the MNPs by the proteins absorbed as part of the corona, the resulting IR spectra were compared.

Degradation of the PC after MNP cellular internalization. To evaluate this degradation, we adopted two experimental approaches. In the first, a fluorescent corona

was constructed by incubating the MNPs in a medium where serum proteins had been previously labeled with a fluorescent dye. The degradation of this fluorescent corona was followed by measuring the fluorescence intensity over time. In the second approach, a protein corona that contained only chicken OVA was generated on APS-MNPs and OVA degradation was analyzed by quantifying the amount of a selected OVA peptide over time by targeted proteomics.

Degradation of the Alexa 488 fluorophore labeled corona. Serum was labeled with a fluorescent reagent and established a fluorescently labeled PC on coated-MNPs as detailed in the Supporting Information. The MNPs were observed by confocal microscopy to follow the degradation of the fluorescent-corona intracellularly. In this experiment, RAW 264.7 or Pan 02 cells were seeded into a 24-well plate at a density of 5×10^4 cells per well and incubated for 24 h at 37 °C. Then, 200 μ l of corona-labeled APS- or DMSA-MNPs were added at a concentration of 125 μ g/ml, and incubated for another 24 and 48 h. The cells were then washed and fixed with 4% paraformaldehyde (PFA) for 15 min, counterstained with DAPI and mounted in the Fluoromount-G medium. Finally, the presence of a fluorescent corona coupled to the MNPs was analyzed on a Leica TCS SP5 (Leica Microsystems) confocal laser scanning microscope with a 63 \times /1.4 NA oil immersion objective. For Alexa 488 (fluorescent corona) quantification, we used Image J software using the intensity measurement.

Degradation of a PC made exclusively from OVA on APS-MNPs, quantifying the amount of a selected OVA peptide over time by targeted proteomics. The process of generating a fluorescent OVA corona on APS-MNPs is explained in the Supporting Information, Supporting Materials and Methods. A confocal microscopy analysis was performed to verify that the OVA corona was still bound to the APS-MNPs once internalized by RAW 264.7 cells (see Supporting Materials and Methods

and Figure S12). To analyze the degradation of the OVA-PC, the selected OVA peptide was quantified over time by targeted proteomics. In this experiment, RAW 264.7 cells (1×10^6 cells/plate) were cultured in 60 mm plates for 24 h and the cells were exposed to APS-MNPs (50 $\mu\text{g/ml}$) functionalized with OVA in culture medium and incubated for 24 h. All the plates were then washed 3 times with PBS to eliminate the non-internalized OVA-APS-MNPs. The samples were then collected to study the degradation process: the first one immediately (0 h), and the following ones at 24, 48 and 72 h after washing. The samples collected were centrifuged at 1200 rpm for 5 minutes and the supernatant removed. The cells were resuspended in protein extraction buffer (50 μl) and incubated in a mixer at 4 °C for 45 min. The resulting suspension was centrifuged at 13,000 rpm at 4 °C for 15 minutes to obtain the protein extracts, which were digested as for the analysis to identify the main OVA peptides and then analyzed in a triple quadrupole type mass spectrometer (model Sciex 5500 QTRAP).

Statistical analysis. All data are presented as the mean \pm standard deviation (SD). One-way and Two-way analysis of variance (ANOVA), Student's and Tukey test were applied to calculate the differences between the values. Values of $p < 0.05$ were considered statistically significant, presented as: * $p < 0.05$, ** $p < 0.01$, and *** $p < 0.001$.

ASSOCIATED CONTENT

*Supporting Information

Supporting Materials and Methods: estimation of the amount of protein that forms the PC and that remains attached to the coatings after washing with a high salt buffer; PrestoBlue cytotoxicity assay; determination of the working concentration for endocytotic inhibitors; comparison of the effect of Filipin III to block MNP internalization with two other inhibitors of caveolae-mediated endocytosis; Prussian Blue staining; fluorescent labeling of serum; establishing a fluorescent labeled PC on coated-MNPs; generating an OVA corona on APS-MNPs; mass spectrometry

determination of OVA peptides; confocal microscopy imaging of internalized APS-MNPs- OVAC. Supporting Results and Discussion: Evaluation of MNP stability: characterization of the stability of MNPs over time. Analysis of the protein composition of the fetal bovine serum: the list of proteins identified in FBS; the most abundant proteins in FBS determined by Label-Free Proteomics; classification of the most abundant proteins in FBS. Analysis of the composition of the PC associated with APS-, DEX- or DMSA-MNPs after incubation in medium containing FBS: variation of the isoelectric point and net charge at different pHs of the main PCs of the APS-MNPs, DEX-MNPs and DMSA-MNPs; table with the statistical analysis of the PC between the MNP coatings and the list of all corona proteins identified and quantified by Label-Free Proteomics. Theoretical calculations from the TG data to see if the relative coating of the APS-MNPs, DEX-MNPs and DMSA-MNPs is sufficient to form a monolayer around the iron oxide core. Estimation of the amount of protein in the PC that remains attached to the coatings after washing with high salt buffer and before infrared analysis of the MNP coatings: percentage of proteins from the PC that remained attached to the MNP coatings after washing with high salt buffer. Cell viability studies to determine the optimal concentration of MNPs and endocytotic inhibitors: Viability of RAW 264.7 macrophages and Pan 02 tumor cells treated with different concentrations of APS-MNPs, DEX-MNPs and DMSA-MNPs; Viability of RAW 264.7 macrophages and Pan 02 tumor cells treated with different concentrations of endocytosis inhibitors as measured with a PrestoBlue assay. Comparison of the effects of Filipin III on MNP internalization with two other inhibitors of caveolae-mediated endocytosis. Analysis of cell uptake of MNPs with different coatings. Protein corona degradation kinetics after cell internalization: optimization of OVA corona formation on APS-MNPs; selection of the main OVA peptides by mass spectrometry; assessment of toxicity, internalization and localization of the APS-MNP-OVAC.

CONFLICT OF INTEREST

The authors have no competing financial interests to declare.

ACKNOWLEDGMENTS

The authors acknowledge the Scientific and Technical Assistance of the Proteomics, Transmission electron microscopy and Confocal microscopy services at the CNB. X-ray diffraction, FTIR spectroscopy and chemical analysis was carried out in the support laboratories of Instituto de Ciencia de Materiales de Madrid (CSIC). We thank Dr Susel del Sol Fernández for the help in analyzing the spectra of the coatings in the degradation study. We also thank Dr Vladimir Mulens Arias for helpful comments on the manuscript. The authors are also grateful to M. Sefton for editing the manuscript for aspects related to the English language. This work was supported by the Spanish Ministerio de Ciencia, Innovación y Universidades, under the following projects:

SAF2017-82223-R to D.F.B., Portilla, Y (FPU15/06170) and Daviu, N (FPU18/04828) received a predoctoral FPU grant from the same Ministry.

AUTHOR INFORMATION

Corresponding Authors

*E-mail: dfbarber@cnb.csic.es (D.F.B.).

ORCID

Y.Portilla: 0000-0003-2738-0384

S. Mellid: 0000-0003-3637-3039

A. Paradela: 0000-0001-6837-7056

A. Ramos: 0000-0002-9716-4110

N. Daviu: 0000-0002-1255-2481

L. Sanz-Ortega: 0000-0003-0413-6311

S. Pérez: 0000-0001-5593-8774

María P. Morales: 0000-0002-7290-7029

D. F. Barber: 0000-0001-8824-5405

REFERENCES

1. Leso, V.; Fontana, L.; Iavicoli, I., Biomedical nanotechnology: Occupational Views. *Nano Today* **2019**, *24*, 10-14.
2. Norouzi, M.; Amerian, M.; Amerian, M.; Atyabi, F., Clinical Applications of Nanomedicine in Cancer Therapy. *Drug Discov Today* **2020**, *25* (1), 107-125.
3. Irvine, D. J.; Dane, E. L., Enhancing Cancer Immunotherapy with Nanomedicine. *Nat Rev Immunol* **2020**, *20* (5), 321-334.
4. Sanz-Ortega, L.; Portilla, Y.; Pérez-Yagüe, S.; Barber, D. F., Magnetic Targeting of adoptively transferred tumour-specific nanoparticle-loaded CD8(+) T cells does not improve their tumour infiltration in a mouse model of cancer but promotes the retention of these cells in tumour-draining lymph nodes. *Journal of nanobiotechnology* **2019**, *17* (1), article 87.
5. Zhi, D.; Yang, T.; Yang, J.; Fu, S.; Zhang, S., Targeting Strategies for Superparamagnetic Iron Oxide Nanoparticles in Cancer Therapy. *Acta Biomaterialia* **2020**, *102*, 13-34.
6. Del Sol-Fernández, S.; Portilla-Tundidor, Y.; Gutiérrez, L.; Odio, O. F.; Reguera, E.; Barber, D. F.; Morales, M. P., Flower-like Mn-Doped Magnetic Nanoparticles Functionalized with $\alpha\beta3$ -Integrin-Ligand to Efficiently Induce Intracellular Heat after Alternating Magnetic Field Exposition, Triggering Glioma Cell Death. *ACS Applied Materials & Interfaces* **2019**, *11* (30), 26648-26663.
7. Vallabani, N. V. S.; Singh, S.; Karakoti, A. S., Magnetic Nanoparticles: Current Trends and Future Aspects in Diagnostics and Nanomedicine. *Current Drug Metabolism* **2019**, *20* (6), 457-472.
8. Cedervall, T.; Lynch, I.; Lindman, S.; Berggård, T.; Thulin, E.; Nilsson, H.; Dawson, K. A.; Linse, S., Understanding the Nanoparticle-Protein Corona Using Methods to Quantify Exchange Rates and Affinities of Proteins for Nanoparticles. *Proc Natl Acad Sci U S A* **2007**, *104* (7), article 2055.
9. Lundqvist, M.; Stigler, J.; Elia, G.; Lynch, I.; Cedervall, T.; Dawson, K. A., Nanoparticle Size and Surface Properties Determine the Protein Corona with Possible

Implications for Biological Impacts. *Proceedings of the National Academy of Sciences* **2008**, *105* (38), 14265-14270.

10. Nguyen, V. H.; Lee, B. J., Protein Corona: a New Approach for Nanomedicine Design. *Int J Nanomedicine* **2017**, *12*, 3137-3151.
11. Barbero, F.; Russo, L.; Vitali, M.; Piella, J.; Salvo, I.; Borrajo, M. L.; Busquets-Fité, M.; Grandori, R.; Bastús, N. G.; Casals, E.; Puentes, V., Formation of the Protein Corona: The Interface between Nanoparticles and the Immune System. *Semin Immunol* **2017**, *34*, 52-60.
12. Yallapu, M. M.; Chauhan, N.; Othman, S. F.; Khalilzad-Sharghi, V.; Ebeling, M. C.; Khan, S.; Jaggi, M.; Chauhan, S. C., Implications of Protein Corona on Physico-chemical and Biological Properties of Magnetic Nanoparticles. *Biomaterials* **2015**, *46*, 1-12.
13. Zhao, J.; Stenzel, M. H., Entry of Nanoparticles Into Cells: the Importance of Nanoparticle Properties. *Polymer Chemistry* **2018**, *9* (3), 259-272.
14. Stepien, G.; Moros, M.; Pérez-Hernández, M.; Monge, M.; Gutiérrez, L.; Fratila, R. M.; las Heras, M. d.; Menao Guillén, S.; Puente Lanzarote, J. J.; Solans, C.; Pardo, J.; de la Fuente, J. M., Effect of Surface Chemistry and Associated Protein Corona on the Long-Term Biodegradation of Iron Oxide Nanoparticles In Vivo. *ACS Applied Materials & Interfaces* **2018**, *10* (5), 4548-4560.
15. Dobrovolskaia, M. A.; Shurin, M.; Shvedova, A. A., Current Understanding of Interactions Between Nanoparticles and the Immune System. *Toxicol Appl Pharmacol* **2016**, *299*, 78-89.
16. Bertoli, F.; Garry, D.; Monopoli, M. P.; Salvati, A.; Dawson, K. A., The Intracellular Destiny of the Protein Corona: A Study on its Cellular Internalization and Evolution. *ACS Nano* **2016**, *10* (11), 10471-10479.
17. Francia, V.; Yang, K.; Deville, S.; Reker-Smit, C.; Nelissen, I.; Salvati, A., Corona Composition Can Affect the Mechanisms Cells Use to Internalize Nanoparticles. *ACS Nano* **2019**, *13* (10), 11107-11121.
18. Mulens-Arias, V.; Rojas, J. M.; Barber, D. F., The Intrinsic Biological Identities of Iron Oxide Nanoparticles and Their Coatings: Unexplored Territory for Combinatorial Therapies. *Nanomaterials (Basel)* **2020**, *10* (5), article 837.
19. Behzadi, S.; Serpooshan, V.; Tao, W.; Hamaly, M. A.; Alkawareek, M. Y.; Dreaden, E. C.; Brown, D.; Alkilany, A. M.; Farokhzad, O. C.; Mahmoudi, M., Cellular Uptake of Nanoparticles: Journey Inside the Cell. *Chem Soc Rev* **2017**, *46* (14), 4218-4244.
20. Iversen, T.-G.; Skotland, T.; Sandvig, K., Endocytosis and Intracellular Transport of Nanoparticles: Present Knowledge and Need for Future Studies. *Nano Today* **2011**, *6* (2), 176-185.
21. Doherty, G. J.; McMahon, H. T., Mechanisms of Endocytosis. *Annual Review of Biochemistry* **2009**, *78* (1), 857-902.
22. Lesniak, A.; Fenaroli, F.; Monopoli, M. P.; Åberg, C.; Dawson, K. A.; Salvati, A., Effects of the Presence or Absence of a Protein Corona on Silica Nanoparticle Uptake and Impact on Cells. *ACS Nano* **2012**, *6* (7), 5845-5857.
23. Treuel, L.; Brandholt, S.; Maffre, P.; Wiegele, S.; Shang, L.; Nienhaus, G. U., Impact of Protein Modification on the Protein Corona on Nanoparticles and Nanoparticle–Cell Interactions. *ACS Nano* **2014**, *8* (1), 503-513.
24. Monopoli, M. P.; Walczyk, D.; Campbell, A.; Elia, G.; Lynch, I.; Baldelli Bombelli, F.; Dawson, K. A., Physical–Chemical Aspects of Protein Corona: Relevance to in Vitro and in Vivo Biological Impacts of Nanoparticles. *Journal of the American Chemical Society* **2011**, *133* (8), 2525-2534.

25. Massart, R., Preparation of Aqueous Magnetic Liquids in Alkaline and Acidic Media. *IEEE Transactions on Magnetics* **1981**, *17* (2), 1247-1248.
26. Tekie, F. S. M.; Hajramezanali, M.; Geramifar, P.; Raoufi, M.; Dinarvand, R.; Soleimani, M.; Atyabi, F., Controlling Evolution of Protein Corona: a Prosperous Approach to Improve Chitosan-Based Nanoparticle Biodistribution and Half-Life. *Scientific Reports* **2020**, *10* (1), article 9664.
27. Maiorano, G.; Sabella, S.; Sorce, B.; Brunetti, V.; Malvindi, M. A.; Cingolani, R.; Pompa, P. P., Effects of Cell Culture Media on the Dynamic Formation of Protein–Nanoparticle Complexes and Influence on the Cellular Response. *ACS Nano* **2010**, *4* (12), 7481-7491.
28. Casals, E.; Pfaller, T.; Duschl, A.; Oostingh, G. J.; Puentes, V. F., Hardening of the Nanoparticle–Protein Corona in Metal (Au, Ag) and Oxide (Fe₃O₄, CoO, and CeO₂) Nanoparticles. *Small* **2011**, *7* (24), 3479-3486.
29. Casalini, T.; Limongelli, V.; Schmutz, M.; Som, C.; Jordan, O.; Wick, P.; Borchard, G.; Perale, G., Molecular Modeling for Nanomaterial-Biology Interactions: Opportunities, Challenges, and Perspectives. *Front Bioeng Biotechnol* **2019**, *7*, article 268.
30. Sakulku, U.; Mahmoudi, M.; Maurizi, L.; Coullerez, G.; Hofmann-Antenbrink, M.; Vries, M.; Motazacker, M.; Rezaee, F.; Hofmann, H., Significance of Surface Charge and Shell Material of Superparamagnetic Iron Oxide Nanoparticle (SPION) Based Core/Shell Nanoparticles on the Composition of the Protein Corona. *Biomaterials Science* **2015**, *3* (2), 265-278.
31. Giri, K.; Shameer, K.; Zimmermann, M. T.; Saha, S.; Chakraborty, P. K.; Sharma, A.; Arvizo, R. R.; Madden, B. J.; McCormick, D. J.; Kocher, J. P.; Bhattacharya, R.; Mukherjee, P., Understanding Protein-Nanoparticle Interaction: a New Gateway to Disease Therapeutics. *Bioconjug Chem* **2014**, *25* (6), 1078-1090.
32. Heberle, H.; Meirelles, G. V.; da Silva, F. R.; Telles, G. P.; Minghim, R., InteractiVenn: a Web-Based Tool for the Analysis of Sets Through Venn Diagrams. *BMC bioinformatics* **2015**, *16* (1), article 169.
33. Shannahan, J. H.; Lai, X.; Ke, P. C.; Podila, R.; Brown, J. M.; Witzmann, F. A., Silver Nanoparticle Protein Corona Composition in Cell Culture Media. *PLOS ONE* **2013**, *8* (9), article e74001.
34. Johnston, B. D.; Kreyling, W. G.; Pfeiffer, C.; Schäffler, M.; Sarioglu, H.; Ristig, S.; Hirn, S.; Haberl, N.; Thalhammer, S.; Hauck, S. M.; Semmler-Behnke, M.; Epple, M.; Hühn, J.; Del Pino, P.; Parak, W. J., Colloidal Stability and Surface Chemistry Are Key Factors for the Composition of the Protein Corona of Inorganic Gold Nanoparticles. *Advanced Functional Materials* **2017**, *27* (42), article 1701956.
35. Xu, M.; Soliman, M. G.; Sun, X.; Pelaz, B.; Feliu, N.; Parak, W. J.; Liu, S., How Entanglement of Different Physicochemical Properties Complicates the Prediction of in Vitro and in Vivo Interactions of Gold Nanoparticles. *ACS Nano* **2018**, *12* (10), 10104-10113.
36. Unterweger, H.; Janko, C.; Schwarz, M.; Dézsi, L.; Urbanics, R.; Matuszak, J.; Örfi, E.; Fülöp, T.; Bäuerle, T.; Szebeni, J.; Journé, C.; Boccaccini, A. R.; Alexiou, C.; Lyer, S.; Cicha, I., Non-Immunogenic Dextran-Coated Superparamagnetic Iron Oxide Nanoparticles: a Biocompatible, Size-Tunable Contrast Agent for Magnetic Resonance Imaging. *Int J Nanomedicine* **2017**, *12*, 5223-5238.
37. Simberg, D.; Park, J. H.; Karmali, P. P.; Zhang, W. M.; Merkulov, S.; McCrae, K.; Bhatia, S. N.; Sailor, M.; Ruoslahti, E., Differential Proteomics Analysis of the Surface Heterogeneity of Dextran Iron Oxide Nanoparticles and the Implications for their In Vivo Clearance. *Biomaterials* **2009**, *30* (23-24), 3926-3933.

38. Schousboe, I., beta 2-Glycoprotein I: a Plasma Inhibitor of the Contact Activation of the Intrinsic Blood Coagulation Pathway. *Blood* **1985**, *66* (5), 1086-1091.
39. Maher, V. M.; Kitano, Y.; Neuwirth, C.; Davies, G. J.; Maseri, A.; Thompson, G. R.; Andreotti, F., Plasminogen Activator Inhibitor-1 Removal Using Dextran Sulphate Columns. Evidence of PAI-1 homeostasis. *J Thromb Thrombolysis* **2009**, *28* (2), 166-172.
40. Zhang, H.; Wu, T.; Yu, W.; Ruan, S.; He, Q.; Gao, H., Ligand Size and Conformation Affect the Behavior of Nanoparticles Coated with in Vitro and in Vivo Protein Corona. *ACS Appl Mater Interfaces* **2018**, *10* (10), 9094-9103.
41. Kreyling, W. G.; Abdelmonem, A. M.; Ali, Z.; Alves, F.; Geiser, M.; Haberl, N.; Hartmann, R.; Hirn, S.; de Aberasturi, D. J.; Kantner, K.; Khadem-Saba, G.; Montenegro, J.-M.; Rejman, J.; Rojo, T.; de Larramendi, I. R.; Ufartes, R.; Wenk, A.; Parak, W. J., In Vivo Integrity of Polymer-Coated Gold Nanoparticles. *Nature Nanotechnology* **2015**, *10* (7), 619-623.
42. Hao, N.; Liu, H.; Li, L.; Chen, D.; Li, L.; Tang, F., In Vitro Degradation Behavior of Silica Nanoparticles Under Physiological Conditions. *J Nanosci Nanotechnol* **2012**, *12* (8), 6346-6354.
43. Kuhn, D. A.; Vanhecke, D.; Michen, B.; Blank, F.; Gehr, P.; Petri-Fink, A.; Rothen-Rutishauser, B., Different Endocytotic Uptake Mechanisms for Nanoparticles in Epithelial Cells and Macrophages. *Beilstein J Nanotechnol* **2014**, *5*, 1625-1636.
44. Ding, L.; Yao, C.; Yin, X.; Li, C.; Huang, Y.; Wu, M.; Wang, B.; Guo, X.; Wang, Y.; Wu, M., Size, Shape, and Protein Corona Determine Cellular Uptake and Removal Mechanisms of Gold Nanoparticles. *Small* **2018**, *14* (42), article e1801451.
45. Ho, Y. T.; Kamm, R. D.; Kah, J. C. Y., Influence of Protein Corona and Caveolae-Mediated Endocytosis on Nanoparticle Uptake and Transcytosis. *Nanoscale* **2018**, *10* (26), 12386-12397.
46. Cheng, X.; Tian, X.; Wu, A.; Li, J.; Tian, J.; Chong, Y.; Chai, Z.; Zhao, Y.; Chen, C.; Ge, C., Protein Corona Influences Cellular Uptake of Gold Nanoparticles by Phagocytic and Nonphagocytic Cells in a Size-Dependent Manner. *ACS Appl Mater Interfaces* **2015**, *7* (37), 20568-20575.
47. Rezaei, G.; Daghighi, S. M.; Raoufi, M.; Esfandyari-Manesh, M.; Rahimifard, M.; Mobarakeh, V. I.; Kamalzare, S.; Ghahremani, M. H.; Atyabi, F.; Abdollahi, M.; Rezaee, F.; Dinarvand, R., Synthetic and Biological Identities of Polymeric Nanoparticles Influencing the Cellular Delivery: An Immunological Link. *J Colloid Interface Sci* **2019**, *556*, 476-491.
48. Forest, V.; Pourchez, J., Preferential Binding of Positive Nanoparticles on Cell Membranes Is Due to Electrostatic Interactions: A Too Simplistic Explanation that Does Not Take Into Account the Nanoparticle Protein Corona. *Mater Sci Eng C Mater Biol Appl* **2017**, *70* (Pt 1), 889-896.
49. Feng, Q.; Liu, Y.; Huang, J.; Chen, K.; Huang, J.; Xiao, K., Uptake, Distribution, Clearance, and Toxicity of Iron Oxide Nanoparticles with Different Sizes and Coatings. *Sci Rep* **2018**, *8* (1), article 2082.
50. Schweiger, C.; Hartmann, R.; Zhang, F.; Parak, W. J.; Kissel, T. H.; Rivera Gil, P., Quantification of the Internalization Patterns of Superparamagnetic Iron Oxide Nanoparticles with Opposite Charge. *J Nanobiotechnology* **2012**, *10*, article 28.
51. Mulens-Arias, V.; Rojas, J. M.; Pérez-Yagüe, S.; Morales, M. P.; Barber, D. F., Polyethylenimine-Coated SPIONs Trigger Macrophage Activation Through TLR-4 Signaling and ROS Production and Modulate Podosome Dynamics. *Biomaterials* **2015**, *52*, 494-506.

52. Mulens-Arias, V.; Rojas, J. M.; Pérez-Yagüe, S.; Morales Mdel, P.; Barber, D. F., Polyethylenimine-Coated SPION Exhibits Potential Intrinsic Anti-Metastatic Properties Inhibiting Migration and Invasion of Pancreatic Tumor Cells. *J Control Release* **2015**, *216*, 78-92.
53. Ma, Y. J.; Gu, H. C., Study on the Endocytosis and the Internalization Mechanism of Aminosilane-Coated Fe₃O₄ Nanoparticles In Vitro. *J Mater Sci Mater Med* **2007**, *18* (11), 2145-2149.
54. Raynal, I.; Prigent, P.; Peyramaure, S.; Najid, A.; Rebutzi, C.; Corot, C., Macrophage Endocytosis of Superparamagnetic Iron Oxide Nanoparticles: Mechanisms and Comparison of Ferumoxides and Ferumoxtran-10. *Invest Radiol* **2004**, *39* (1), 56-63.
55. Lunov, O.; Zablotskii, V.; Syrovets, T.; Röcker, C.; Tron, K.; Nienhaus, G. U.; Simmet, T., Modeling Receptor-Mediated Endocytosis of Polymer-Functionalized Iron Oxide Nanoparticles by Human Macrophages. *Biomaterials* **2011**, *32* (2), 547-555.
56. Hansen, C. G.; Nichols, B. J., Molecular Mechanisms of Clathrin-Independent Endocytosis. *J Cell Sci* **2009**, *122* (11), 1713-1721.
57. Yan, Y.; Gause, K. T.; Kamphuis, M. M. J.; Ang, C.-S.; O'Brien-Simpson, N. M.; Lenzo, J. C.; Reynolds, E. C.; Nice, E. C.; Caruso, F., Differential Roles of the Protein Corona in the Cellular Uptake of Nanoporous Polymer Particles by Monocyte and Macrophage Cell Lines. *ACS Nano* **2013**, *7* (12), 10960-10970.
58. Ritz, S.; Schöttler, S.; Kotman, N.; Baier, G.; Musyanovych, A.; Kuharev, J.; Landfester, K.; Schild, H.; Jahn, O.; Tenzer, S.; Mailänder, V., Protein Corona of Nanoparticles: Distinct Proteins Regulate the Cellular Uptake. *Biomacromolecules* **2015**, *16* (4), 1311-1321.
59. Ashby, J.; Pan, S.; Zhong, W., Size and Surface Functionalization of Iron Oxide Nanoparticles Influence the Composition and Dynamic Nature of Their Protein Corona. *ACS Applied Materials & Interfaces* **2014**, *6* (17), 15412-15419.
60. Jiang, W.; Kim, B. Y. S.; Rutka, J. T.; Chan, W. C. W., Nanoparticle-Mediated Cellular Response Is Size-Dependent. *Nature Nanotechnology* **2008**, *3* (3), 145-150.
61. Ma, N.; Ma, C.; Li, C.; Wang, T.; Tang, Y.; Wang, H.; Mou, X.; Chen, Z.; He, N., Influence of Nanoparticle Shape, Size, and Surface Functionalization on Cellular Uptake. *Journal of Nanoscience and Nanotechnology* **2013**, *13* (10), 6485-6498.
62. Palchetti, S.; Pozzi, D.; Capriotti, A. L.; Barbera, G. L.; Chiozzi, R. Z.; Digiacomo, L.; Peruzzi, G.; Caracciolo, G.; Laganà, A., Influence of Dynamic Flow Environment on Nanoparticle-Protein Corona: From Protein Patterns to Uptake in Cancer Cells. *Colloids and Surfaces B: Biointerfaces* **2017**, *153*, 263-271.
63. Fleischer, C. C.; Payne, C. K., Nanoparticle–Cell Interactions: Molecular Structure of the Protein Corona and Cellular Outcomes. *Accounts of Chemical Research* **2014**, *47* (8), 2651-2659.
64. Wang, F.; Yu, L.; Monopoli, M. P.; Sandin, P.; Mahon, E.; Salvati, A.; Dawson, K. A., The Biomolecular Corona Is Retained During Nanoparticle Uptake and Protects the Cells from the Damage Induced by Cationic Nanoparticles Until Degraded in the Lysosomes. *Nanomedicine* **2013**, *9* (8), 1159-1168.
65. de la Presa, P.; Luengo, Y.; Multigner, M.; Costo, R.; Morales, M. P.; Rivero, G.; Hernando, A., Study of Heating Efficiency as a Function of Concentration, Size, and Applied Field in γ -Fe₂O₃ Nanoparticles. *The Journal of Physical Chemistry C* **2012**, *116* (48), 25602-25610.

66. Luengo, Y.; Nardecchia, S.; Morales, M. P.; Serrano, M. C., Different Cell Responses Induced by Exposure to Maghemite Nanoparticles. *Nanoscale* **2013**, *5* (23), 11428-11437.
67. Shevchenko, A.; Wilm, M.; Vorm, O.; Mann, M., Mass Spectrometric Sequencing of Proteins Silver-Stained Polyacrylamide Gels. *Anal Chem* **1996**, *68* (5), 850-858.
68. Ramos-Fernández, A.; Paradela, A.; Navajas, R.; Albar, J. P., Generalized Method for Probability-Based Peptide and Protein Identification from Tandem Mass Spectrometry Data and Sequence Database Searching. *Mol Cell Proteomics* **2008**, *7* (9), 1748-1754.
69. Lopez-Serra, P.; Marcilla, M.; Villanueva, A.; Ramos-Fernandez, A.; Palau, A.; Leal, L.; Wahi, J. E.; Setien-Baranda, F.; Szczesna, K.; Moutinho, C.; Martinez-Cardus, A.; Heyn, H.; Sandoval, J.; Puertas, S.; Vidal, A.; Sanjuan, X.; Martinez-Balibrea, E.; Viñals, F.; Perales, J. C.; Bramsem, J. B.; Ørntoft, T. F.; Andersen, C. L.; Tabernero, J.; McDermott, U.; Boxer, M. B.; Heiden, M. G. V.; Albar, J. P.; Esteller, M., A DERL3-Associated Defect in the Degradation of SLC2A1 Mediates the Warburg Effect. *Nature Communications* **2014**, *5* (1), article 3608.